Contents lists available at ScienceDirect

Chemical Engineering Research and Design

journal homepage: www.elsevier.com/locate/cherd

Real-time furnace balancing of steam methane reforming furnaces

Anh Tran[a], *Madeleine Pont*[a], *Marquis Crose*[a], *Panagiotis D. Christofides*[a,b,*]

[a] *Department of Chemical and Biomolecular Engineering, University of California, Los Angeles, CA 90095-1592, USA*
[b] *Department of Electrical and Computer Engineering, University of California, Los Angeles, CA 90095-1592, USA*

ARTICLE INFO

Article history:
Received 26 February 2018
Received in revised form 19 March 2018
Accepted 20 March 2018
Available online 13 April 2018

Keywords:
Steam methane reforming
CFD modeling
Data-based modeling
Process optimization
Furnace balancing

ABSTRACT

This paper focuses on the development of a real-time furnace-balancing scheme for a reformer at a centralized hydrogen facility using steam methane reforming (SMR) technology so that the reformer fuel input can be optimized in real-time to increase the plant throughput and to reject operational disturbances associated with flow control valves. Initially, the framework for the furnace-balancing scheme, the statistical-based model identification and the valve-to-flow-rate converter developed in Tran et al. (2017a, 2018) are integrated with a heuristic search algorithm to create a real-time balancing procedure, which recursively calculates different total fuel flow rates of which the respective spatial distribution to burners is optimized until key operational specifications, e.g., the reformer throughput is maximized, and the outer tube wall temperature (OTWT) along the reforming tube length of all reforming tubes must not exceed the design temperature of the reforming tube wall, are satisfied. Subsequently, a com;1;putational fluid dynamic (CFD) model of the reformer developed in Tran et al. (2017b) is used to represent the on-line unit at the SMR-based hydrogen facility and is used to characterize the previously unstudied dynamic behavior of the reformer, based on which we develop an optimal strategy to implement the optimized total fuel flow rate to maximize the reformer throughput. Finally, a case study in which the balancing procedure is implemented on the reformer initially operated under the nominal reformer input is proposed, and the results are used to demonstrate that the furnace-balancing scheme successfully determines the optimized reformer fuel input to increase the reformer throughput while meeting the OTWT limits.

1. Introduction

High levels of atmospheric carbon dioxide, which is a known consequence of extensive use of fossil fuels as the primary sources of energy in the last century, are adversely affecting climate patterns across the world. In a global effort to reduce carbon emissions to mitigate some of the effects of climate change stricter emissions regulations have passed, which have motivated the need for alternative fuels such as hydrogen. A vision of a carbon-emission-free and sustainable energy system shared by many (Balat, 2008; Lemus and Duart, 2010) is aligned with a future hydrogen economy, in which hydrogen gas is used as a transportation fuel. This is because a hydrogen economy holds the potential to allow a nation to achieve energy security, i.e., to become independent of the limited and constantly depleting foreign crude oil supplies and on political stability of countries with large crude oil reservoirs, and to resolve some effects of climate change without halting

* *Corresponding author at*: Department of Chemical and Biomolecular Engineering, University of California, Los Angeles, CA 90095-1592, USA.
E-mail address: pdc@seas.ucla.edu (P.D. Christofides).
https://doi.org/10.1016/j.cherd.2018.03.032

economic growth. This vision of a carbon-emission-free and sustainable hydrogen economy is viable because hydrogen gas can be synthesized from a myriad of commercial thermal pathways (e.g., steam reforming, partial oxidation, gasification, cracking, pyrolysis, and biological reactions) that start from a diverse array of primary energy sources including fossil fuels, biomass and renewable energy. Additionally, physical and chemical properties, e.g., a high diffusivity, a high specific energy content and a wide range of flammability, of hydrogen gas make it an efficient transportation fuel. For instance, hydrogen gas can diffuse rapidly into air to create a uniform combustible mixture while releasing 2.75 times greater heat of combustion per unit mass than hydrocarbon fuels (Balat, 2008).

In addition to the vision of a carbon-emission-free and sustainable hydrogen economy, the current demand for hydrogen gas is large, e.g., the annual world-wide hydrogen production in 2008 was ~500 billion Nm^3, which is equivalent to 44.5 million metric tons, and corresponded to a global market of more than $40 billion. The demand for hydrogen is also expected to grow at an annual rate of 5–10% because hydrogen gas is widely used as precursor across a variety of manufacturing industries. For example, fertilizer (ammonia), petroleum refinery and methanol plants are responsible for 49%, 37% and 8% of world-wide hydrogen consumption, respectively (Balat, 2008). Thus, solving challenges encountered in commercial production of hydrogen and optimizing the production line has become of particular interest to both academia and industry.

It is noted that although hydrogen gas can be derived from a diverse array of primary energy sources with a variety of commercial processes, only a few are economically feasible. With current state-of-the-art technology, hydrogen gas is produced almost exclusively from fossil fuels, e.g., ~96% of the world-wide hydrogen production activity uses fossil fuels as starting materials (Balat, 2008), by thermochemical processes. Specifically, steam methane reforming (SMR), an endothermic conversion of methane and superheated steam into hydrogen gas, carbon monoxide and carbon dioxide, is by far the most common commercial hydrogen production process. In 2007, SMR was responsible for the largest share (e.g., 80–85%) of the world-wide hydrogen production (Simpson and Lutz, 2007). The reasons for the prevalent usage of centralized SMR-based facilities to meet the large and growing demand for hydrogen gas are twofold: (1) SMR can achieve up to 90% thermal efficiency on the metric of high heating value (Peng, 2012) and up to 82% of methane conversion (Ding and Alpay, 2000), and (2) centralized SMR-based facilities with the production rates over 1 million Nm^3 per day are reported to require the least capital investment (Barreto et al., 2003) and have a low production cost (e.g., $6.90 per gigajoule (GJ)) compared to hydrogen plants that use competing technologies, e.g., the production cost via electrolysis can be as high as $98 per GJ (Lemus and Duart, 2010). In practice, the process is simultaneously catalyzed and carried out under high operating temperatures inside hundreds of nickel-based catalyst filled tubular reactors to achieve a high conversion of methane in a finite packed-bed length, which allows the SMR-based facilities to become economically viable. To create the high temperature environment necessary to achieve a high conversion of methane, the reforming tubes are housed inside an insulated combustion chamber where the recycled effluent from the purification units and the fresh natural gas are burnt in excess air. At SMR-based hydrogen plants, the hydrogen-producing units, i.e., the reformers, are the most expensive equipment in terms of the maintenance and operating costs compared to other major equipment such as the hydrotreating, prereforming, water-shift and purification units. For instance, the re-tubing cost of the reformer is ~10% of the total capital investment (Latham et al., 2011), and the annual investment to procure fresh natural gas for a SMR-based hydrogen plant with a production rate of 2.7 million Nm^3 per day is $62 million (Latham et al., 2011). Therefore, a higher reformer efficiency is expected to lower the reformer operating cost and improve the plant efficiency, which results in significant financial benefits (Kumar et al., 2015; Tran et al., 2017a; Latham et al., 2011).

The investigation reported in Tran et al. (2017a) suggests that the conversion of methane via SMR in the reformer operated under varying spatial distributions of the fixed total fuel flow rate are the same. This finding suggests that the reformer throughput can only be increased by increasing the reformer firing rate, which is, however, constrained by the physical limitation of the reforming tube wall material. This is because the degradation of the microstructure of the reforming tube wall due to temperature aging accelerates, if the outer tube wall temperature (OTWT) at any location along the reforming tube length exceeds its design value (Guan et al., 2005; Alvino et al., 2010; Gong et al., 1999). Specifically, the evolution of the microstructure of the reforming tube wall starting from precipitation of primary and secondary carbides in the austenitic matrix, which leads to creep cavitation damage presented in the form of isolated cavities and coalesce cavities, followed by the formation of microcracks which propagate to form macrocracks occurs in an accelerated timeline leading to premature failure of the reforming tubes. For instance, the service life of the reforming tubes is reduced by half under an operating condition that allows the maximum OTWT to exceed its design value by 20 K for an extended period of time (Pantoleontos et al., 2012). Therefore, real-time measurement of the OTWTs of the reforming tubes is expected to provide an accurate means to monitor the reformer service life. For this reason, the SMR-based hydrogen facility uses a system of infrared cameras to periodically sample the OTWTs of the reforming tubes at a few discrete locations along the reforming tube length through peepholes that are integrated into the refractory wall lining; each set of measurements collected at the fixed height is typically defined as an OTWT distribution. Experimental plant data of OTWT distributions have revealed that the OTWTs within each OTWT distribution are nonuniform with a fluctuating range between 30 K and 110 K (Kumar et al., 2015), and OTWT profiles along the reforming tube length vary noticeably among the reforming tubes. This nonuniformity in OTWT distributions poses a major challenge in the estimation of the optimized firing rate due to the high risk of accelerating the degradation of the microstructure of the reforming tube wall. Specifically, the maximum OTWT along the reforming tube length among all reforming tubes in the reformer operated under a suboptimal fuel distribution can be higher than that in a reformer operated under an optimized fuel distribution with the same total fuel flow rate (Tran et al., 2017a). Consequently, the optimized firing rate may not be implemented without the proper distribution of the optimized total fuel flow rate, and the SMR-based hydrogen plant throughput is compromised to retain the reformer service life and to reduce the risk of suffering substantial capital and production losses.

In addition to the challenges associated with the estimation of the optimized firing rate imposed by the physical

limitation of the reforming tube wall material and the inherent nonuniformity in the OTWT distributions, the unstudied dynamic response of the reformer under load alterations poses an additional challenge in the implementation of the optimized firing rate due to the sensitivity of the reforming tube service life to the operating temperature. Specifically, it is believed that the furnace-side temperature is expected to increase immediately in response to a positive step change in the total fuel flow rate due to the rapid combustion of the furnace-side fuel coupled with fast thermal radiative heat transfer in the high temperature combustion chamber. However, it remains unclear that if the additional fired duty can be transferred to the tube-side mixture at a sufficient overall rate that would prevent the OTWTs from exceeding the respective steady-state values due to the thermal resistance of the nickel-based catalyst pellets, which are made from an alumina oxide ceramic material with relatively low thermal conductivity. As a result, there is a possibility that a large positive step change in the total fuel flow rate designed to achieve the optimized firing rate may cause the OTWTs of some reforming tubes to temporarily exceed its design temperature causing the degradation of the microstructure of the reforming tube wall to accelerate, which leads to premature failure of the reformer. Hence, designing a robust systematic operating method (i.e., the furnace-balancing scheme) that identifies the optimized firing rate and the corresponding strategic implementation of the maximum total fuel flow rate without accelerating the degradation of the microstructure of the reforming tube wall is of great interest to the hydrogen manufacturing industry.

Motivated by this, the present work utilizes a statistical-based model identification and the furnace-balancing framework to design a real-time robust furnace-balancing scheme that simultaneously identifies the optimized total fuel flow rate and its corresponding optimized valve distribution such that the reformer throughput is maximized within the physical limitation of the reforming tube wall material. Subsequently, the work utilizes the high-fidelity computational fluid dynamic (CFD) model for the reformer to investigate the unstudied dynamic response of the reformer during load alterations to propose a strategic implementation of the optimized total fuel flow rate without causing additional damage to the reforming tubes in the process. The remainder of this manuscript is structured as follows: Section 2 presents a high-level description of the furnace-balancing scheme of which the major components and the basic workflow are introduced, Section 3 details the development of the reformer CFD model (Tran et al., 2017b) to justify using the reformer CFD model to represent the on-line reformer at the SMR-based hydrogen facility, Sections 4 and 5 present the key findings, features and capabilities of the statistical-based model identification (Tran et al., 2018) and the valve-to-flow-rate converter (Tran et al., 2017a) to highlight their utilities for real-time optimization of the reformer to improve the plant-wise energy efficiency and to reject operational disturbances associated with flow control valves, Section 6 introduces readers to the development of a sequential workflow that aims to increase the reformer throughput by maximizing the total fuel flow rate, i.e., the reformer firing rate, without sacrificing the reformer service life in the process, and Section 7 addresses the computational challenges associated with the steady-state and transient simulations of the reformer CFD model and the derivation of the data-driven model for the OTWT distribution to emphasize the importance of parallel computing for the purpose of determining the optimized reformer fuel input in real-time using the proposed approach. Finally, in Section 8, the goodness-of-fit of the data-driven model for the OTWT distribution is evaluated to justify the use of the model in the development of the balancing procedure, the dynamic response of the reformer to two deterministic step changes in the total fuel flow rate from its nominal value is analyzed to design an appropriate strategy to implement the optimized firing rate estimated by the balancing procedure, and the performance of the furnace-balancing is presented to demonstrate the effectiveness of the proposed approach.

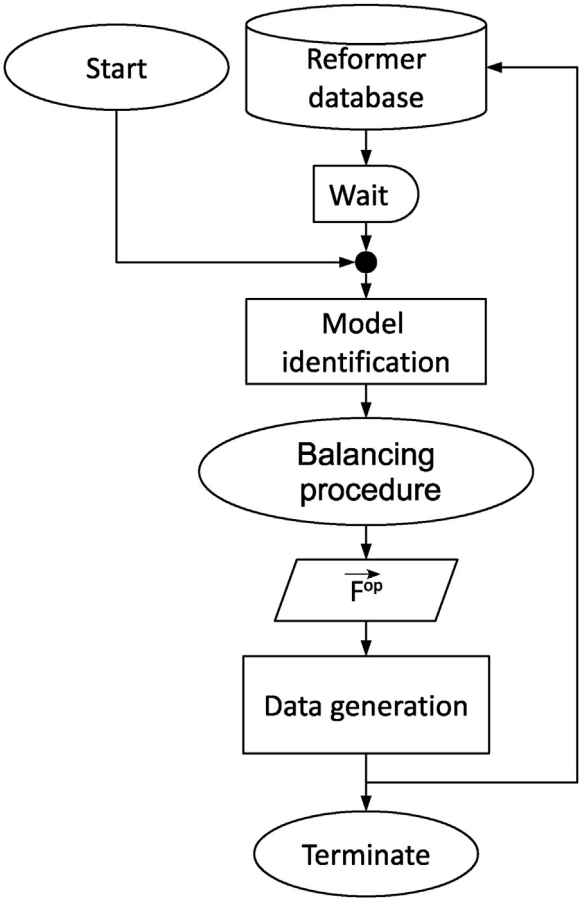

Fig. 1 – Flowchart of the furnace-balancing scheme.

2. Overview of the furnace-balancing scheme

In the present work, the integrated furnace-balancing scheme that simultaneously calculates the maximum total fuel mass flow rate and the corresponding optimized valve distribution (which together are referred to as the optimized reformer fuel input) such that the conversion of methane via SMR is maximized, and the maximum OTWT along the reforming tube length among all reforming tubes is strictly less than its design temperature to avoid causing the reforming tubes to fail prematurely is presented for the first time. To this end, the framework for the furnace-balancing scheme that was proposed in Tran et al. (2017a), which was used to reduce the temperature nonuniformity inside the combustion chamber at the fixed nominal total fuel flow rate, is utilized in this work. The furnace-balancing scheme is redesigned as shown in Fig. 1, which makes use of the statistical-based model identification, the valve-to-flow-rate converter, the balancing procedure and the high-fidelity reformer CFD model.

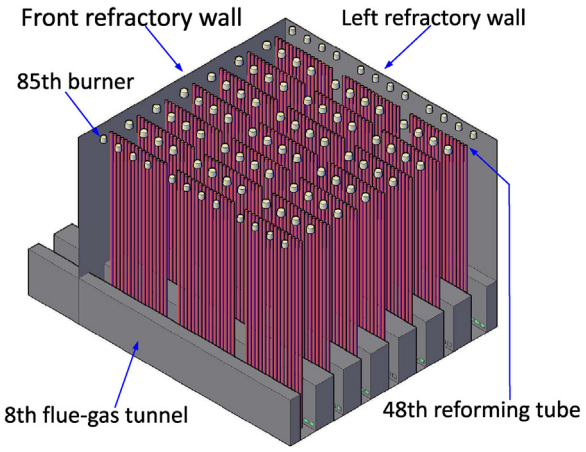

Fig. 2 – Isometric view of the reformer in which the right and back refractory walls are made transparent to display the interior components. The reformer includes 336 reforming tubes (represented by 336 cylinders), 96 burners (represented by 96 frustum cones), and 8 flue-gas tunnels (represented by 8 rectangular intrusions).

Initially, it begins with the statistical-based model identification to derive the data-driven model for the OTWT distribution from the reformer database. Next, it integrates the most up-to-date data-driven model in the balancing procedure to find the optimized reformer fuel input that abides the aforementioned operational specifications. Subsequently, it implements the optimized reformer fuel input as the burner boundary conditions of the reformer CFD model using the strategy designed from the investigation of the transient response of the reformer during load alterations (presented in Section 8.2). In the remainder of this manuscript, the key developments and features of our previous work will be revisited in Sections 3–5 in an effort to provide readers with sufficient background, and the development of the balancing procedure will be detailed at great length in Section 6 for the purpose of clarity.

3. Reformer CFD model

The high-fidelity reformer CFD model that was first proposed in Tran et al. (2017b) and further developed in Tran et al. (2017a) is a key component of the furnace-balancing scheme and is used to represent the on-line reformer at a commercial SMR-based hydrogen plant. This assumption will be justified by examining the geometry, mesh and development of the reformer CFD model.

The geometry of the reformer CFD model is drawn with a 3D computer-aided design tool and based on the blueprint of the physical counterpart so that it contains all of the important features of the on-line reformer, i.e., seven rows of 48 12.5-m long reforming tubes, six rows of 12 inner-lane burners, two rows of 12 outer-lane burners and eight elongated flue-gas tunnels with extraction ports. Indeed, the reformer geometry as shown in Fig. 2 adequately depicts a 16 m × 16 m × 13 m hydrogen producing unit at the SMR-based hydrogen plant. Readers with interest in the structural design and detailed layout of the reformer are advised to study our previous work (Tran et al., 2017b).

In addition to the accurate representation of the reformer geometry, the mesh of the reformer CFD model was well crafted. Specifically, during the developing phase of the reformer model (Tran et al., 2017b) the generation of the reformer mesh was prioritized because accuracy of converged solutions generated by CFD models depends on the mesh quality. For example, a CFD model created from an insufficiently dense and poor quality mesh is expected to yield inaccurate or even unphysical solutions, and it is also expected to require a higher computational cost compared to CFD models built from a high quality mesh at the same resolution. In Tran et al. (2017b), we initially provided an in-depth review of two different mesh generation procedures, in which their advantages and disadvantages were studied under the same premise using the reformer geometry, based on which we concluded that the multi-block structured hexahedral mesh generation procedure was more appropriate. Then, we used ANSYS ICEM to create the hexahedral reformer mesh that was characterized to have an acceptable mesh quality. In particular, the reformer mesh has the high averaged orthogonal factor and low averaged ortho skew, which indicate that the mesh has a small number of distorted cells, and the reformer mesh also has the in-range minimum orthogonal factor, in-range max ortho skew and in-range max aspect ratio, which indicate that the distorted cells in the reformer mesh are not expected to cause convergence difficulties. Finally, we carried out a grid-independent study, and we found that the reformer mesh consisting of ~41 million cells allows the reformer CFD model to produce grid-independent solutions. We note that readers who are interested in our rationale for using the multi-block structured hexahedral mesh generation procedure and additional descriptions of the reformer mesh are advised to study our previous work (Tran et al., 2017b,a).

Furthermore, we tailored the ANSYS Fluent model to simulate the known transport phenomena and chemical reactions associated with SMR and the air-combustion process as noted in Section 1. Specifically, the effects of turbulence in the furnace-side flow on the transport phenomena, chemical reactions and transport variables associated with the air-combustion process are modeled by the Reynolds-averaged Navier–Stokes (RANS) and Boussinesq hypothesis using the standard $k-\epsilon$ model coupled with the enhanced wall treatment (EWT) function. We note that the use of the EWT function in the turbulence model has been shown to improve the accuracy of CFD solutions in the near-wall regions for low-Reynolds number meshes. The air-combustion process is modeled by adding source terms in the convective-diffusive species material balances, which are computed using the premixed combustion assumption, the global kinetic model of methane-air combustion (Nicol, 1995), the global kinetic model of hydrogen-air combustion (Bane et al., 2010) and the finite rate/eddy dissipation (FR/ED) turbulence-chemistry interaction model. Thermal radiative heat transfer within the furnace side between outer walls of reforming tubes, walls of the flue-gas tunnels, refractory walls of the combustion chamber and the furnace-side flow is modeled by adding a source term in the convective-diffusive energy balance, which is computed by the discrete ordinate method, temperature-independent wall emissivity coefficients and the thermal absorptivity of the furnace-side flow. In addition, the thermal absorptivity of the furnace-side flow in the reformer CFD model is assumed to be temperature dependent and modeled by the empirical correlation of the furnace-side thermal emissivity (Maximov, 2012), Lambert Beer's law and Kirchoff's law. In the tube side, the effects of turbulence in the tube-side flow on the transport phenomena, chemical reactions and transport variables associated with SMR are also modeled

by the RANS and Boussinesq hypothesis using the standard $k-\epsilon$ model with the EWT function. The reforming tubes are modeled by the pseudo-homogeneous reactor model, i.e., a continuum approach in which the solid phase is not explicitly modeled and is assumed to co-exist in thermal equilibrium with the fluid phase throughout the reactor volume, using the ANSYS Fluent porous zone function with a void fraction factor of 0.609. The reforming tube wall is modeled by the thin wall model (Lao et al., 2016). SMR is modeled by adding source terms in the convective-diffusive species material balances, which are computed using the global kinetic model of SMR (Xu and Froment, 1989), the FR/ED model, the catalyst packing factor and the effectiveness factor. We note that the use of the effectiveness factor is critical for accurate simulations of the methane conversion via SMR because it allows the effects of the external mass transfer limitation (as superheated steam and methane must be transferred from the tube-side bulk flow to the external surface of the catalyst pellets) and internal mass transfer limitation (as the reactants must diffuse through the support material to reach the metal active site) on the chemical reaction rates associated with SMR to be simulated. In addition, physical and chemical properties of tube-side and furnace-side species are imported from ANSYS Fluent database, based on which properties of the furnace-side and tube-side flows are computed using appropriate models. For instance, the molecular thermal conductivities and molecular viscosities of the furnace-side and tube-side flows are calculated using ideal-gas mixing law, while the diffusion coefficients of the furnace-side and tube-side flows are calculated using the kinetic theory. Moreover, reforming tubes, catalyst pellets, walls of the combustion chambers and walls of the flue-gas tunnels are assumed to be made of appropriate materials and are encoded all physical properties (e.g., density, thermal conductivity, specific heat capacity and emissivity coefficient) reported in the SMR literature. For example, reforming tubes are typically made from cast creep resistant austenitic steel HP grade, and its catalyst pellets are typically made from nickel-based catalyst dispersed in alpha alumina support. Readers who are interested in our rationales for the proposed modeling strategies for the reformer CFD model, the two-step converging strategy and the data collecting procedure are recommended to study our previous work (Tran et al., 2017b).

The steady-state simulation results generated by the reformer CFD model, whose boundary conditions are modified based on an operating information of the on-line reformer provided by our third party industry collaborator, have been shown to be consistent with typical plant data in the SMR literature and with the plant historian data. Therefore, the reformer CFD model can adequately represent the on-line unit, and simulation results generated by the reformer model, whose boundary conditions are modified based on varying fuel distributions and total fuel flow rates, can be considered to be reliable estimates of the plant data obtained from the on-line unit at equivalent operating conditions. As a result, it is reasonable to use the reformer CFD model to represent the on-line reformer, so that it can be used to study the transient response of the on-line reformer when the total fuel flow rate is increased and to demonstrate the effectiveness of the integrated furnace-balancing scheme.

It is worth noting that at the commercial-scale SMR-based hydrogen plant, the inputs to the furnace side of the reformer are regulated by a system of flow control valves, the OTWTs at a finite number of locations along the reforming tubes inside the furnace are continuously monitored by a system of infrared cameras through peepholes, the synthesis gas composition can be sampled, and the historian data of the on-line reformer are well documented. Therefore, in an effort to simulate a realistic on-site investigation we assume that we have access to the historian data, i.e., the reformer database, which can be reasonably assumed to be a collection of simulation results generated by the reformer model. In this study, the reformer database is populated with 26 steady-state solutions generated by the reformer CFD model under 26 different reformer fuel inputs (Tran et al., 2017a,b). For each data point, only information about the valve positions of all flow control valves, the total fuel flow rate, the fuel flow rates of all burners, the composition of the synthesis gas and the OTWTs of all reforming tubes at a distance 6.5 m away from the reformer ceiling will be utilized, so that the reformer database and the historian plant data collected from the on-line reformer at the SMR-based hydrogen plant are essentially equivalent. The reformer database will be utilized extensively by the statistical-based model identification to create a computationally efficient data-driven model for the reformer controlled variables (i.e., the OTWT distribution) as a function of the reformer manipulated inputs (i.e., the flow control valve distribution and the total fuel flow rate), which will be detailed in the upcoming section.

4. Statistical-based model identification

The statistical-based model identification that was proposed in Tran et al. (2018) is a key component of the furnace-balancing scheme and is used to create a computationally efficient data-driven model for the OTWT distribution as a function of the flow control valve distribution and the total fuel flow rate from the reformer database in an effort to find the optimized reformer fuel input in real-time. The model identification is designed to simultaneously execute two model building processes for each OTWT, i.e., the prediction and correction steps, which create two corresponding data-driven models, namely, the prediction and correction models, respectively. As a result, the prediction and correction estimates of the ith OTWT are computed based on the fuel flow rate distribution and based on the OTWTs of the nearby reforming tubes, respectively.

It is important to note that although the reformer has 96 distinct burners, we have found that the OTWT of the ith reforming tube depends primarily on the fuel flow rates of the nearby burners. This is because more than 95% of the energy absorbed by the reforming tubes is transferred to the outer tube walls by thermal radiation (Tran et al., 2018; Olivieri and Vegliò, 2008), while the intensity of thermal radiation decreases with increasing distance between the heat source (i.e., the burners) and the heat sink (i.e., the reforming tubes). Therefore, the model building process for the ith prediction model is designed to iteratively screen for the important predictors for the ith OTWT using Bayesian variable selection, Occam's window, sparse non-linear regression with 11 transformation functions, Bayesian information criterion (BIC) and a first-principles model for thermal radiation. In addition, the model building process is designed to keep tabs on all sub-prediction models for the ith OTWT (which are defined as the data-driven models derived for the purpose of screening for the important predictors) with high goodness of fit, each of which is expected to adequately explain the non-linearity in

the dependence of the ith OTWT on its predictors and can be expressed as follows,

$$\tilde{T}_{i,k}^{P,n} = \sum_{g=1}^{11} \hat{\alpha}_i^{kg} f_g\left(\vec{F}^n|_{S_{iR}^k}\right) + \hat{\alpha}_i^k \quad (1)$$

where $\tilde{T}_{i,k}^{P,n}$ is an estimate of the ith OTWT computed from the kth sub-prediction model for the ith OTWT ($M_{i,k}^P$) and the nth fuel distribution ($\vec{F}^n$), S_{iR}^k and $f_g(\cdot)$ are the set of predictors and the gth transformation function used in the identification of $M_{i,k}^P$ by sparse non-linear regression, respectively, $\vec{F}^n|_{S_{iR}^k}$ is the reduced-order nth fuel distribution such that it only retains the fuel flow rates of burners associated with S_{iR}^k, $\hat{\alpha}_i^{kg}$ is the estimated parameter vector corresponding to $f_g(\cdot)$ in $M_{i,k}^P$ and $\hat{\alpha}_i^k$ is the estimated ambient temperature in $M_{i,k}^P$. The 11 transformation functions in sparse non-linear regression are designed to be nonnegative monotonically increasing functions as follows,

$$f_1\left(\vec{F}^n\right) = \left[F_1^n, F_2^n, \ldots, F_{96}^n\right]^T \quad (2a)$$

$$f_2\left(\vec{F}^n\right) = \left[(F_1^n)^2, (F_2^n)^2, \ldots, (F_{96}^n)^2\right]^T \quad (2b)$$

$$f_3\left(\vec{F}^n\right) = \left[(F_1^n)^3, (F_2^n)^3, \ldots, (F_{96}^n)^3\right]^T \quad (2c)$$

$$f_4\left(\vec{F}^n\right) = \left[\sqrt[2]{F_1^n}, \sqrt[2]{F_2^n}, \cdots, \sqrt[2]{F_{96}^n}\right]^T \quad (2d)$$

$$f_5\left(\vec{F}^n\right) = \left[\sqrt[3]{F_1^n}, \sqrt[3]{F_2^n}, \ldots, \sqrt[3]{F_{96}^n}\right]^T \quad (2e)$$

$$f_6\left(\vec{F}^n\right) = \left[\sqrt[4]{F_1^n}, \sqrt[4]{F_2^n}, \ldots, \sqrt[4]{F_{96}^n}\right]^T \quad (2f)$$

$$f_7\left(\vec{F}^n\right) = \left[\sqrt[5]{F_1^n}, \sqrt[5]{F_2^n}, \ldots, \sqrt[5]{F_{96}^n}\right]^T \quad (2g)$$

$$f_8\left(\vec{F}^n\right) = \left[\exp\left(F_1^n\right), \exp\left(F_2^n\right), \ldots, \exp\left(F_{96}^n\right)\right]^T \quad (2h)$$

$$f_9\left(\vec{F}^n\right) = \left[\sqrt[6]{F_1^n}, \sqrt[6]{F_2^n}, \ldots, \sqrt[6]{F_{96}^n}\right]^T \quad (2i)$$

$$f_{10}\left(\vec{F}^n\right) = \left[\sqrt[10]{F_1^n}, \sqrt[10]{F_2^n}, \ldots, \sqrt[10]{F_{96}^n}\right]^T \quad (2j)$$

$$f_{11}\left(\vec{F}^n\right) = \left[\sqrt[15]{F_1^n}, \sqrt[15]{F_2^n}, \ldots, \sqrt[15]{F_{96}^n}\right]^T, \quad (2k)$$

which is inspired by the observed response of the ith OTWT to varying reformer fuel inputs. For examples, when the fuel flow rates of the predictors for the ith OTWT are increased, the ith OTWT increases. Furthermore, three additional transformation functions (Eqs. (2i), (2j) and (2k)) are incorporated into the library proposed in Tran et al. (2018) (Eqs. (2a)–(2h)) to improve the goodness of fit and forecasting accuracy of the ith prediction model for a wider range of reformer fuel inputs. In an effort to prevent presumptuous bias from being introduced in the derivation of the ith prediction model by our arbitrary choice of the hyperparameter (i.e., LASSO parameter) of sparse non-linear regression, cross-validation methods are used to select the optimized LASSO parameter based on the reformer database. Specifically, Section 8.1 will demonstrate the importance of using the optimized LASSO parameter by showing that a LASSO parameter larger than the optimized value allows the model building process to favor underfitting sub-prediction models, while a LASSO parameter smaller than the optimized value allows the model building process to favor overfitting sub-prediction models. Subsequently, instead of treating the "best" sub-prediction model derived from the complete set of important predictors as the ith prediction model, the prediction step combines the ith sub-prediction models with high goodness of fit to derive the ith prediction model using Bayesian model averaging (BMA) and BIC in an effort to account for uncertainty in model selection (Hoeting et al., 1999). Specifically, the ith prediction model (M_i^P) is formulated as the weighted sum of the ith sub-prediction models as follows,

$$\hat{T}_i^{P,n} = \sum_{k=1}^{K_i} w_{i,k}^P \tilde{T}_{i,k}^{P,n} \quad (3)$$

where $\hat{T}_i^{P,n}$ is the prediction estimate of the ith OTWT computed from M_i^P and $\vec{F}^n$, K_i is the number of sub-prediction models with high model goodness of fit for the ith OTWT and $w_{i,k}^P$ is the BMA weighting factor of $M_{i,k}^P$. Then, a collection of all prediction models arranged in an ascending order of reforming tube IDs is used to define the prediction model for the OTWT distribution (M^P) as follows,

$$\hat{\vec{T}}^{P,n} = \begin{pmatrix} \hat{T}_1^{P,n} \\ \hat{T}_2^{P,n} \\ \vdots \\ \hat{T}_{336}^{P,n} \end{pmatrix} \quad (4)$$

where $\hat{\vec{T}}^{P,n}$ is the prediction estimate of the OTWT distribution computed from M^P and $\vec{F}^n$.

In Tran et al. (2018), we have recognized that OTWTs of neighboring reforming tubes are spatially correlated. Therefore, the model building process for the ith correction model is designed to compute the sample correlation (i.e., the sample semivariograms) among the OTWTs of the reforming tubes in a sufficiently large, predefined neighborhood from the reformer database using the classical estimator. Then, a theoretical semivariogram model is fitted based on the sample semivariograms using the method of weighted least squares (Cressie, 1985). In an effort to prevent presumptuous bias from being introduced in the derivation of the ith correction model by an ad-hoc and subjective eyeballing approach to select the theoretical semivariogram model, cross-validation methods are used to select the optimized theoretical semivariogram model from a collection of four potential models proposed in Tran et al. (2018). Then, the model building process uses the theoretical semivariogram model to derive the ith correction model using ordinary Kriging modeling. Specifically, the ith correction model (M_i^C) is formulated as the weighted sum of prediction estimates of OTWTs in the ith Kriging neighborhood (denoted as $\mathbf{W}_i^K$), which contain at most three nearest northward, one nearest eastward, three nearest southward

and one nearest westward neighbors of the ith reforming tube, as follows,

$$\hat{T}_i^{C,n} = \sum_j^{w_i^K} w_{i,j}^C \hat{T}_j^{P,n} \tag{5}$$

where $\hat{T}_i^{C,n}$ is a correction estimate of the ith OTWT computed from M_i^C and the prediction estimates of OTWTs in $\mathbf{W}_i^K$ ($\hat{T}_j^{P,n}$), and $w_{i,j}^C$ is the Kriging weighting factor corresponding to jth reforming tube. Then, a collection of all correction models arranged in an ascending order of reforming tube IDs is used to define the correction model for the OTWT distribution (M^C) as follows,

$$\hat{\vec{T}}^{C,n} = \begin{pmatrix} \hat{T}_1^{C,n} \\ \hat{T}_2^{C,n} \\ \vdots \\ \hat{T}_{336}^{C,n} \end{pmatrix} \tag{6}$$

where $\hat{\vec{T}}^{C,n}$ is the correction estimate of the OTWT distribution computed from M^C and $\vec{F}^n$. Finally, the data-driven model for the OTWT distribution (M) is formulated as the weighted average of M^P and M^C as follows,

$$\hat{\vec{T}}^n = w^P \hat{\vec{T}}^{P,n} + (1 - w^P)\hat{\vec{T}}^{C,n} \tag{7}$$

where w^P is the hyperparameter of M of which an optimized value is estimated by cross-validation methods from a set of 21 possible values, i.e., $\mathbf{S}_w = \{0.00, 0.05, 0.10, \ldots, 0.95, 1.00\}$, based on the reformer database. The resulting data-driven model for the OTWT distribution, of which hyperparameters are optimized to minimize out-of-sample prediction errors, incorporates the information about uncertainty in model selection and the spatial correlations in OTWTs among the neighboring reforming tubes into estimating the OTWT distribution based on the fuel flow rate distribution. It is worth noting that the data-driven model for the OTWT distribution is a system of algebraic equations and has been shown to yield estimates of the OTWT distribution for varying reformer fuel inputs instantaneously on a single core machine of the shared computing cluster at UCLA. This feature allows the furnace-balancing procedure, which will be detailed in Section 6, to search for the optimal reformer fuel input in real-time.

5. Valve-to-flow-rate converter

The valve-to-flow-rate converter that was developed in Tran et al. (2017a) is an important component of the furnace-balancing scheme and is used to make our present work a more realistic representation of an on-site investigation, where the reformer fuel input is regulated by a system of manual flow control valves, so that our findings can be brought into practice with little or no changes. It is important to note that fuel lines to burners, of which fuel flow rates are regulated by the flow control valves, are interconnected through a header fuel system with a main header fuel inlet and eight sub-headers fuel pipes as detailed in Kumar et al. (2015). This structural design allows the excess fuel feed of burners in overheating regions to be redistributed by partially closing the flow control valves of the corresponding fuel lines. The converter model developed based on the material conservation law as shown in Eq. (8) can capture this characteristic through the system of coupled algebraic equations.

In the development of the converter, the following assumptions are made and translated into appropriate mathematical formulations. Two adjacent fuel lines to burners within each burner row are assumed to be regulated by a flow control valve, which forces the fuel flow rates of the associated burners to be the same. The structural layout of the system of manual flow control valves in the reformer can be depicted in an information matrix [Y] as shown in Eq. (9c). Next, fuel lines to burners are assumed to be regulated by two types of linear flow control valves with different maximum capacities corresponding to inner-lane and outer-lane burners. The arrangement and identity of burners in the reformer can be captured in an information matrix [X] as shown in Eq. (9d). Finally, the pressure of fuel feed in the header fuel system of the reformer is assumed to be sufficiently high so that there will be no backflow for all valve distributions. The model for the converter is formulated as follows,

$$\vec{F} = \delta[X] \cdot [Y] \cdot \vec{V} \tag{8}$$

$$\vec{V} \in \mathbb{R}^{48\times 1} \tag{9a}$$

$$\vec{F} \in \mathbb{R}^{96\times 1} \quad F_i \geq 0 \forall i \in [1, 96] \tag{9b}$$

$$\begin{aligned} &[Y] \in \mathbb{R}^{96\times 48} \\ &\quad Y_{i,j} = 1.0; \quad i = 2j-1 \cup i = 2j \text{ where } j \in [1, 48] \\ &\quad Y_{i,j} = 0.0; \quad i \neq 2j-1 \cap i \neq 2j \text{ where } j \in [1, 48] \end{aligned} \tag{9c}$$

$$\begin{aligned} &[X] \in \mathbb{R}^{96\times 96} \\ &\quad X_{i,j} = 0.6; \quad i = j \text{ where } i \in [1, 12] \cup [85, 96] \\ &\quad X_{i,j} = 1.0; \quad i = j \text{ where } i \in [13, 84] \\ &\quad X_{i,j} = 0.0; \quad i \neq j \end{aligned} \tag{9d}$$

$$\delta = \frac{F_{tot}}{\|[X] \cdot [Y] \cdot \vec{V}\|_1} \tag{9e}$$

where δ is the valve-to-flow-rate proportionality coefficient and $\vec{V}$ is the valve distribution. In this work, we define $\vec{V}$ as the collection of the percent open positions of all flow control valves in the reformer. The converter allows us to formulate the furnace-balancing scheme to use the valve distribution as the manipulated variables as in the on-line reformer, so that the optimized solution generated from our study can be directly applied to the on-line unit to distribute the fuel feed among all burners. The converter also gives us an opportunity to examine the transient response and steady-state behavior of the reformer when the reformer is subjected to common valve related disturbances. It is important to note that the model for the converter allows a fuel distribution to be generated from different valve distributions (which will be discussed in Section 6.1); however, these valve distributions are not equivalent in practice. Specifically, among valve distributions that yield the same fuel flow rate distribution, those that deviate further from the fully open valve setting require the fuel feed to the reformer to be at a higher pressure which corresponds to higher operating cost. This information will be used in the formulation of the model-based balancing procedure, which will be detailed in the upcoming section.

6. Balancing procedure

The balancing procedure is the core component of the furnace-balancing scheme and is used to search for the optimized total fuel flow rate and the corresponding valve distribution such that the conversion of methane via SMR is maximized, and the maximum OTWT along the reforming tube length among all reforming tubes is strictly less than the design temperature of the reforming tube wall material. The balancing procedure is a sequential workflow system, as shown in Fig. 3, of which major components are the data-driven model for the OTWT distribution, the valve-to-flow-rate converter and the furnace-balancing optimizer. It is designed to assess the nonuniformity of the current temperature distribution inside the combustion chamber by means of the estimated OTWT distribution calculated from the current valve distribution (denoted as $\vec{V}^0$) and total fuel flow rate (denoted as F^0_{tot}) using the valve distribution analyzer. Specifically, $\vec{V}^0$ and F^0_{tot} are used as inputs for the converter to generate the current fuel distribution (denoted as $\vec{F}^0$), which is used as an input for M to estimate the current OTWT distribution (denoted as $\hat{\vec{T}}^0$). The assumption that $\hat{\vec{T}}^0$ is a good representation of the current temperature distribution inside the reformer can be justified because the plant data of the initial OTWT distribution (denoted as $\vec{T}^0$) belongs to the reformer database from which M is derived, and M is expected to have a high goodness of fit. Next, $\hat{\vec{T}}^0$ is processed by the OTWT distribution analyzer, which identifies the maximum value in the OTWT distribution as follows,

$$\hat{T}^{max}_{wall,i} = \left\| \begin{pmatrix} \hat{T}^i_1 \\ \hat{T}^i_2 \\ \vdots \\ \hat{T}^i_{336} \end{pmatrix} \right\|_\infty \tag{10}$$

where $\hat{T}^{max}_{wall,i}$ is the estimated maximum value of the ith OTWT distribution and i is 0. Then, $\hat{T}^{max}_{wall,0}$ is used as an input for the furnace-balancing search indicator, which produces a binary search indicator (denoted as F_I) as follows,

$$F_I = 1.0, \quad \hat{T}^{max}_{wall,0} < T^{max,*}_{wall} \tag{11}$$

$$F_I = -1.0, \quad \hat{T}^{max}_{wall,0} \geq T^{max,*}_{wall} \tag{12}$$

where $T^{max,*}_{wall}$ is the maximum allowable OTWT and is a user-specified parameter of the furnace-balancing scheme (a systematic method to estimate $T^{max,*}_{wall}$ will be discussed in Section 8.3). Subsequently, F_I is used to guide the heuristic search algorithm that recursively applies incremental changes to the total fuel flow rate followed by evaluating the impact of the adjusted total fuel flow rate on the maximum value of the OTWT distribution, and based on which it reformulates the future action to meet the operational specifications in a finite number of steps. Specifically, $F_I = 1.0$ implies that the total fuel mass flow rate can be increased to increase the methane conversion via SMR, while $F_I = -1.0$ implies that the total fuel mass flow rate must be decreased to avoid causing the reforming tubes to fail prematurely.

In this effort, the heuristic search algorithm is structured to have two sequential modes (referred as the aggressive and conservative modes, respectively) with an identical framework, which begins with the flow rate generator followed by the furnace-balancing optimizer, valve distribution analyzer and furnace-balancing analyzer. In particular, the aggressive search is responsible for identifying the neighborhood of the optimal total fuel flow rate, and the conservative search is responsible for identifying the optimized value such that the operational specifications are satisfied. For instance, when the value of F_I is 1.0, the heuristic search algorithm begins with the aggressive flow rate generator, which recursively applies "large" increments to the total fuel flow rate to approximate the "smallest" upper-bound value, which is defined as the minimum total fuel flow rate that allows the maximum value of the OTWT to exceed $T^{max,*}_{wall}$, as follows,

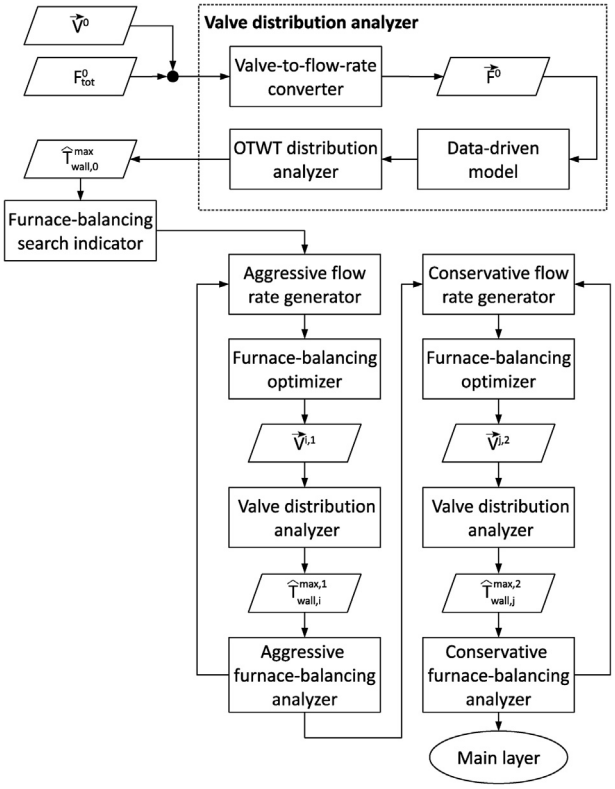

Fig. 3 – Flowchart of the balancing procedure.

$$F^{i,1}_{tot} = F^0_{tot}(1.0 + i\delta_{01}F_I), \quad \text{where} \quad i = 1, 2, 3, \ldots \tag{13}$$

where $\delta_{01} = 10\%$ is the parameter of the aggressive search, $F^{i,1}_{tot}$ is the adjusted total fuel flow rate at the ith iteration in the aggressive search and $i = 1$ is the index of the first iteration. In the ith iteration, $F^{i,1}_{tot}$ is used as an input for the furnace-balancing optimizer which optimizes the valve distribution so that the nonuniformity in the OTWT distribution is minimized. Then, $F^{i,1}_{tot}$ and the corresponding optimized valve distribution (denoted by $\vec{V}^{i,1}$) are used as inputs to the valve distribution analyzer to estimate the maximum value in the corresponding OTWT distribution (denoted by $\hat{T}^{max,1}_{wall,i}$) as discussed previously. Finally, $\hat{T}^{max,1}_{wall,i}$ is used as an input to the aggressive furnace-balancing analyzer, which determines if $F^{i,1}_{tot}$ can be considered to be an approximation of the smallest upper-bound value of the total fuel flow rate. Specifically, when $\hat{T}^{max,1}_{wall,i}$ begins to exceed $T^{max,*}_{wall}$, the aggressive furnace-balancing analyzer classifies $F^{i,1}_{tot}$ as an approximation of the smallest upper-bound value, which is labeled as $F^{*,1}_{tot}$, and terminates the aggressive search.

After the approximation of the smallest upper-bound value is obtained, the heuristic search algorithm continues with the conservative flow rate generator, which gradually applies "small" decrements to the upper-bound value until the reformer returns back into the safe operating regime as follows,

$$F_{tot}^{j,2} = F_{tot}^{*,1}(1.0 - j\delta_{02}F_I) \quad \text{where} \quad j = 1, 2, 3, \ldots \tag{14}$$

where δ_{02} = 1% is the parameter of the conservative search, $F_{tot}^{j,2}$ is the adjusted total fuel flow rate at the jth iteration in the conservative search and j = 1 is the index of the first iteration. After $F_{tot}^{j,2}$ is computed, an analogous procedure as described in the aggressive search, which begins with the furnace-balancing optimizer followed by the valve distribution analyzer, is executed. Then, the maximum value (denoted by $\hat{T}_{wall,j}^{max,2}$) in the OTWT distribution estimated from $F_{tot}^{j,2}$ and the corresponding optimized valve distribution (denoted by $\vec{V}^{j,2}$) in the jth iteration of the conservative search is used as an input to the conservative furnace-balancing analyzer, which determines if $F_{tot}^{j,2}$ can be considered to be the optimized total fuel flow rate. Specifically, when $\hat{T}_{wall,j}^{max,2}$ begins to drop below $T_{wall}^{max,*}$, which indicates that the operational specifications are satisfied, the conservative furnace-balancing analyzer classifies $F_{tot}^{j,2}$ as the optimized total fuel flow rate, which is labeled as F_{tot}^{op}, and terminates the conservative search. Finally, F_{tot}^{op} and the corresponding optimized valve distribution (denoted by $\vec{V}^{op}$) are translated into the optimized fuel distribution (denoted by $\vec{F}^{op}$), which is strategically applied as the reoptimized burner boundary conditions for the reformer CFD model so that the reforming tubes do not suffer additional damage during the transition to achieve the optimized reformer firing rate.

On the contrary, when the value of F_I is −1.0, the search direction is reversed. Specifically, the aggressive flow rate generator recursively applies "large" decrements to the total fuel flow rate as shown in Eq. (13) to approximate the "largest" lower-bound value, which is defined as the maximum total fuel flow rate that allows the maximum value of the OTWT to approximate $T_{wall}^{max,*}$ from the right. Then, the conservative search gradually applies "small" increments to the lower-bound value as shown in Eq. (14) until $\hat{T}_{wall,j}^{max,2}$ begins to exceed $T_{wall}^{max,*}$ indicating that the reformer is leaving the safe operating regime, and at this point, the conservative furnace-balancing analyzer classifies $F_{tot}^{j-1,2}$ as F_{tot}^{op}, and terminates the conservative search. Similarly, F_{tot}^{op} and $\vec{V}^{op}$ are translated into $\vec{F}^{op}$, which is applied as the reoptimized burner boundary conditions for the reformer CFD model. The heuristic search algorithm proposed in this study can derive F_{tot}^{op}, $\vec{V}^{op}$ and $\vec{F}^{op}$ from any arbitrary initial reformer fuel input so that the operational specifications are satisfied.

6.1. *Furnace-balancing optimizer*

The furnace-balancing optimizer that was developed in Tran et al. (2017a) is of the uttermost importance in the heuristic search algorithm and is reformulated to be fully capable of optimizing the valve distribution at any total fuel flow rate to reduce the nonuniformity in the OTWT distribution. Specifically, the improved optimizer aims to minimize the sum of weighted squared differences between the OTWTs at a location 6.5 m away from the reformer celling of all reforming tubes and an "ideal" OTWT at a given total fuel flow rate to allow the reformer to be operated under the optimal condition in which the OTWT profiles along the reforming tube length of all reforming tubes are identical. In this subsection, a means to estimate the ideal OTWT at any total fuel flow rate is presented followed by the discussion of the development of a more robust objective function for the furnace-balancing optimizer.

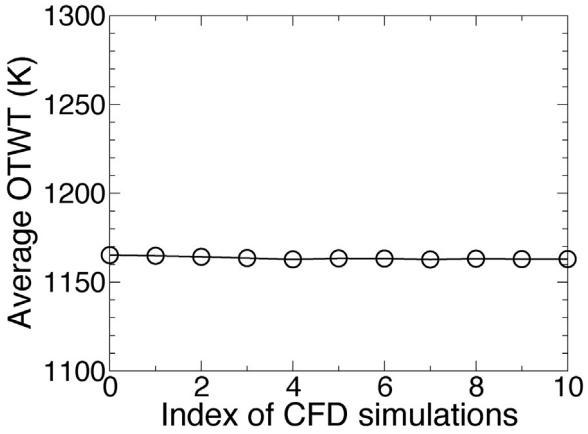

Fig. 4 – Average value of the OTWT distribution when the reformer is operated under the nominal fuel flow rate and varying valve distributions.

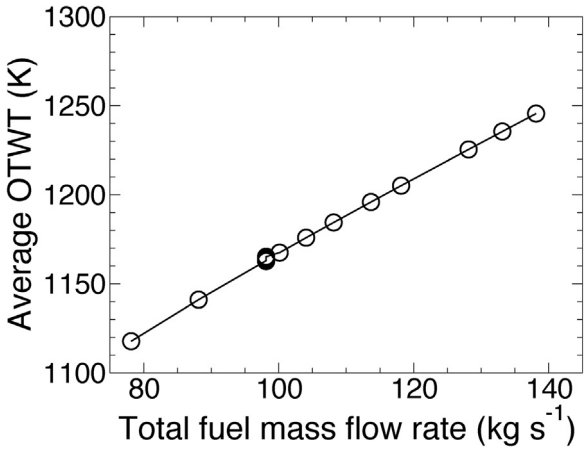

Fig. 5 – Average value of the OTWT distribution when the reformer is operated under varying fuel flow rates and varying valve distributions.

A thorough analysis of the results reported in Tran et al. (2017a) suggests that the average value of the OTWT distribution (denoted by T_{wall}^{ave}) is a good estimator of the ideal OTWT because it is invariant with respect to the valve distribution under a fixed total fuel flow rate. Therefore, the relationship between T_{wall}^{ave} and total fuel flow rate is analyzed by using the reformer database. In particular, Fig. 4 shows that T_{wall}^{ave} is, indeed, independent of the valve distribution under a fixed total fuel flow rate, and Fig. 5 shows that T_{wall}^{ave} exhibits a strong linear correlation to the total fuel flow rate. Therefore, we can create an estimator for the ideal OTWT as a function of the total fuel flow rate by fitting a linear function using ordinary least squares (OLS) to the plant data presented in Fig. 5. The result of the fit is,

$$\hat{T}_{wall}^{ave} = 2.09F_{tot} + 957.62. \tag{15}$$

Subsequently, the furnace-balancing optimizer is formulated using the data-driven model for the OTWT distribution (Eq. (7)), the valve-to-flow-rate converter (Eq. (8)), the estimator for

the ideal OTWT (Eq. (15)) and the total fuel flow rate (denoted by F^{i}_{tot}, which is generated by the flow rate generators of the heuristic search algorithm). Specifically, it is written as a program with the quadratic cost function that aims to minimize the sum of weighted squared deviations of the OTWTs in the OTWT distribution from its average value by optimizing the percent open positions of the functional control valves. The quadratic cost function of the furnace-balancing optimizer has the following form,

$$\min_{\substack{V_j \in [60\%,\,100\%] \\ j \in [1,48]\backslash \mathbf{S}_{def}}} \sum_{k=1}^{336} w_k \left(\hat{T}^{ave}_{wall,i} - \hat{T}^{i}_{k}\right)^2 \tag{16}$$

where $V^{u}_{j} = 100\%$ and $V^{l}_{j} = 60\%$ are the upper and lower bounds of the percent opening position of the jth flow control valve, respectively, $\mathbf{S}_{def}$ is the set that contains indices of the defective flow control valves, w_k is the weighting factor of the kth reforming tube (which is has been discussed at length in Tran et al. (2017a) and will not be elaborated further in this manuscript for brevity), $\hat{T}^{ave}_{wall,i}$ and $\hat{T}^{i}_{k}$ are the estimated average OTWT and the estimated kth OTWT, respectively, in the OTWT distribution. It is worth noting that only in a scenario which all flow control valves are functional, and the cardinality of $\mathbf{S}_{def}$ is zero, an optimized valve distribution (denoted by $\vec{V}^{op}$) calculated by the furnace-balancing optimizer is expected to have multiple equivalent solutions as discussed in Section 5. This statement can be mathematically rationalized by first using the model for the converter to solve for $\vec{V}^{op}$ from the optimized fuel distribution (denoted by $\vec{F}^{op}$) as follows,

$$F^{op}_{2j} = F^{op}_{2j-1} = \delta^{op} X_{2j,2j} Y_{2j,j} V^{op}_{j} \quad \text{where} \quad j = 1, 2, \ldots, 48 \tag{17a}$$

$$\delta^{op} = \frac{\sum_{i=1}^{96} F^{op}_{i}}{\|[X]\cdot[Y]\cdot\vec{V}^{op}\|_1} \tag{17b}$$

where F^{op}_{2j} and F^{op}_{2j-1} are the optimized fuel flow rates of the $(2j)$th and $(2j-1)$th burners respectively, $X_{2j,2j}$ is the element of the $(2j)$th row and $(2j)$th column in $[X]$, $Y_{2j,j}$ is the element of the $(2j)$th row and jth column in $[Y]$ and V^{op}_{j} is the optimized percent opening position of the jth flow control valve. Then, the system of non-linear algebraic equations as shown in Eq. (17) can be transformed into a system of linear algebraic equations by taking the ratio of all equations in Eq. (17a) to an arbitrarily selected equation as follows,

$$\frac{F^{op}_{2j}}{F^{op}_{2k}} = \frac{X_{2j,2j} Y_{2j,j} V^{op}_{j}}{X_{2k,2k} Y_{2k,k} V^{op}_{k}} \quad \text{where} \quad j = 1, 2, \ldots, 48 \text{ and } j \neq k. \tag{18}$$

It is evident that the system of linear algebraic equations, in which the percent opening positions of the flow control valves are the unknowns, as shown in Eq. (18) is underdetermined and is expected to have multiple solutions. However, these valve distributions are by no means the same in a sense of the plant-wise energy efficiency as explained in Section 5, and therefore, the valve distribution that deviates the least from the fully open valve setting is considered as the true and unique optimized solution. The task of finding such valve distribution is achieved with the valve optimizer which is developed by exploiting the linear relationship between the percent opening position of the linear flow control valve and the fuel flow rates that it regulates, and the assumption that the flow control valve to which the maximum fuel flow rate corresponds is fully open. The valve optimizer is formulated as follows,

$$V^{op}_{j.eq} = \frac{\left(\delta^{op}[X][Y]\vec{V}^{op}\right)_{2j}}{X_{2j,2j}\|\delta^{op}[X][Y]\vec{V}^{op}\|_\infty} \tag{19}$$

where $V^{op}_{j.eq}$ is the equivalent optimized percent open position of the jth flow control valve, $\left(\delta^{op}[X][Y]\vec{V}^{op}\right)_{2j}$ is the fuel flow rate of the $(2j)$th burner, and $\|\delta^{op}[X][Y]\vec{V}^{op}\|_\infty$ is the maximum fuel flow rate among all burners. The equivalent optimized valve distribution is expected to simultaneously minimize the sum of the weighted squared deviations of all OTWTs in the OTWT distribution from the ideal OTWT, which is computed based on the given total fuel flow rate, and minimizes the required duty of the upstream compression system, and therefore, improves the energy efficiency of the SMR-based hydrogen plant.

7. Parallel processing

In this section, the computational challenges associated with the steady-state and transient simulations of the reformer CFD model under varying reformer fuel inputs and the derivation of the data-driven model for the OTWT distribution from the reformer database are discussed. Specifically, in all simulations of the reformer CFD model, the furnace-side and tube-side domains are discretized into ~41 million control volumes, and in each of which the reformer mathematical model (i.e., a high dimensional system of non-linear partial integro-differential equations with seven independent variables Mishra and Prasad, 1998) is numerically solved or integrated forward in time by the finite volume method. It is evident that the random access memory (RAM), e.g., 32 GB, and the processing speed of a standard high performance workstation are insufficient to keep track of values of transport variables in all control volumes and to compute the numerical solutions of the reformer mathematical model in all control volumes in a practical time frame. In addition, the derivation of M can be viewed as an ensemble of 336 independent model building processes for 336 distinct OTWTs. Each model building process can be viewed as a sub-ensemble of two independent model building processes, i.e., the prediction and correction steps, in which cross validation methods are used to select the optimized hyperparameters to improve the forecasting accuracy of M. To better comprehend the magnitude of the number of computing tasks needed to derive M from the reformer database, we consider the derivation of the data-driven model reported in Tran et al. (2018) as an illustrative example. Specifically, 18 training data sets were used to create the reformer database, and leave-out-one (LOO) cross validation was used to select the optimal lasso parameter from a predefined set of 18 possible LASSO parameters and to select the optimal theoretical semivariogram model from a collection of four potential models. Given this premise, the model building process for the OTWT distribution is expected to require more than 120,000 computing tasks (which will be elaborated at the end of this section), each of which requires the minimum CPU clock time of 10 min, which corresponds to a total CPU clock time of ~2.3 years. This evidence shows that serial processing on a standard work station is unfit to derive M in a practical time frame. As a result, all simulations of the reformer CFD model and the derivation of M are executed on the Hoffman2 computing cluster at UCLA.

In this work, we designate 7 private-access high performance compute nodes with the total processing power of 128 cores and system memory of 1640 GB for simulations of the reformer CFD model. Under ANSYS Fluent parallel architecture, the CFD solver uses a core as a host process to create a communication pathway between the CFD solver and the graphical user interface (GUI) of an instance of ANSYS Fluent, and the remaining cores as computing-node processes to numerically calculate the solutions of the Navier–Stoke equations, energy balance and species balances in all control volumes. It is important to note that ANSYS Fluent parallel architecture allows the compute-node processes to be fully linked, so that they can effectively communicate, synchronize and perform global reductions via ANSYS Fluent message-passing interface (MPI). Next, the CFD solver uses the automatic mesh partition and load balancing function to divide the reformer mesh into 127 parts corresponding to the number of compute-node processes followed by assigning a different mesh partition to each compute-node process. Then, 127 compute-node processes simultaneously use the finite volume method to express the reformer mathematical model within each control volume of their respective assigned partitions in the form of algebraic equations by using divergence theorem and second order upwind interpolation algorithm, which are numerically solved. At the end of each iteration, 127 compute-node processes synchronize to calculate the global normalized residuals of all conserved variables, which are used as indicators for the steady-state CFD solver to terminate and for the transient CFD solver to advance to the next time step. We note that the steady-state solutions and transient solutions of the reformer CFD model executed on 7 private-access high performance compute nodes on the Hoffman2 computing cluster using ANSYS Fluent parallel solver can be obtained within a day and 60 days, respectively.

In addition, we exploit the intrinsically distributed structure of the statistical-based model identification and designate our shared computational resources on the Hoffman2 computing cluster to derive M from the reformer data, of which optimized hyperparameters are selected by two times 10-fold cross validation (CV) method. To this end, a massive number of computing tasks are submitted to the job scheduler of the Hoffman2 cluster, which automatically and optimally dispatches computing tasks. Specifically, 336 job arrays, each of which hosts 460 independent model building processes for the ith CV prediction models are submitted to identify the optimized LASSO parameters for the derivations of the prediction models. Simultaneously, 336 additional job arrays, each of which hosts 80 independent model building processes for the ith CV correction models are submitted to identify the optimized theoretical semivariogram model for the derivations of the correction models. Subsequently, 336 computing tasks for deriving the "forecasting" prediction models and 336 additional computing tasks for deriving the "forecasting" corrections models using the respective optimized hyperparameters are submitted to the job scheduler. Finally, 420 computing tasks for identifying the optimized value of w^P of M are submitted to the job scheduler. The resulting data-driven model for the OTWT distribution, of which hyperparameters are optimized to improve forecasting accuracy using two times 10-fold CV method, can be obtained within a day on the shared computing cluster. Additionally, in the event that new steady-state measurements of the OTWT distribution inside the reformer become available, they can always be integrated into the reformer database, and M can be retrained in real-time. The ability to perform on-line model reidentification is due to the distributed structure of the statistical-based model identification, the availability of the high performance computing cluster and the justifiable use of the previously optimized hyperparameters. Thus, this feature allows the balancing procedure to utilize the most up-to-date data-driven model at all times so that the optimized reformer fuel input is always the most optimal solution.

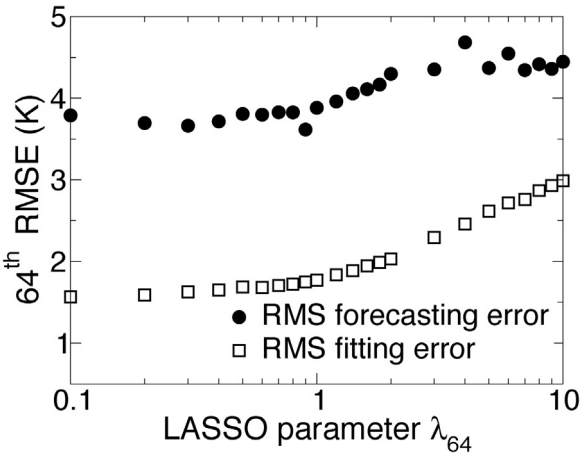

Fig. 6 – RMS fitting and forecasting errors associated with the proposed values of λ_{64} generated from the two times 10-fold cross-validation study in the derivation of M_{64}^P are plotted in empty squares and black circles, respectively.

8. Simulation results

8.1. *Validation of data-driven model for the OTWT distribution*

In this subsection, the results generated from two times 10-fold cross-validation studies in the derivation of the data-driven model for the OTWT distribution from the reformer database are used to demonstrate the importance of using the optimized hyperparameters for obtaining accurate estimations of the OTWT distribution. To this end, we consider the derivation of the prediction and correction models for two representative OTWTs, namely, 65th and 161st OTWTs, of reforming tubes in two distinct local environments, which are characterized based on their respective proximity to the combustion chamber wall. The results of the cross-validation studies in the derivation of M_{64}^P and M_{161}^P are presented in Figs. 6 and 7 based on which the corresponding optimized LASSO parameters are chosen. Figs. 6 and 7 show that choosing an arbitrarily small LASSO parameter to allow the sparse non-linear regression to favor minimizing the CV fitting errors tends to result in overfitting models, which are indicated by small CV fitting errors and large CV forecasting errors. To the contrary, choosing an arbitrarily large LASSO parameter to allow that sparse non-linear regression to favor minimizing the model complexity tends to result in underfitting models, which are indicated by large CV fitting errors and large CV forecasting errors. Next, the results of the cross validation studies in the derivations of M_{64}^C and M_{161}^C are presented in Figs. 8 and 9, based on which the corresponding optimized theoretical semivariogram models are chosen. Figs. 8 and 9 show that an incorrect choice of the theoretical semivariogram model to describe the spatial correlation in OTWTs in the Kriging neighborhood can have a detrimental impact

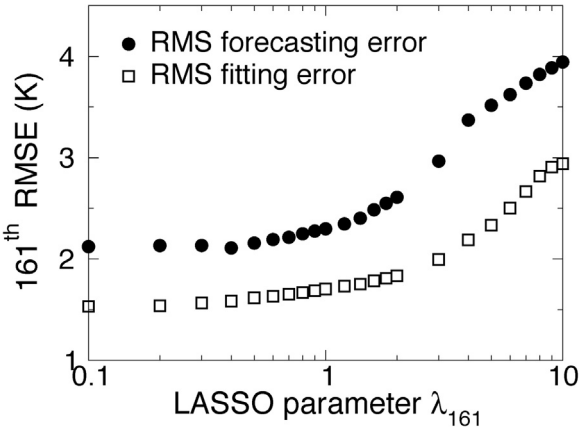

Fig. 7 – RMS fitting and forecasting errors associated with the proposed values of λ_{161} generated from the two times 10-fold cross-validation study in the derivation of M^{P}_{161} are plotted in empty squares and black circles, respectively.

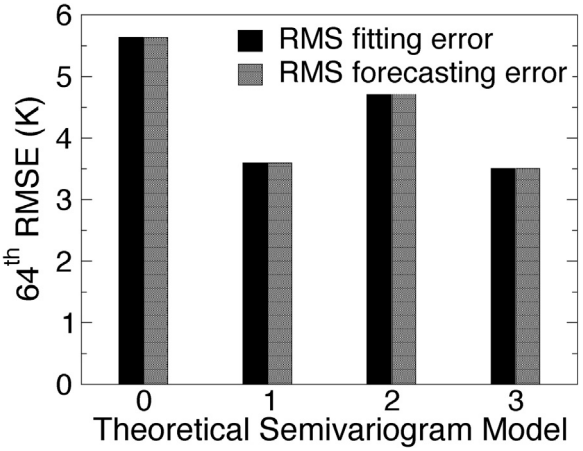

Fig. 8 – RMS fitting and forecasting errors associated with each of the four theoretical semivariogram models (given on the horizontal axis as 0, 1, 2, and 3, which correspond to linear omnidirectional, linear anisotropic, exponential omnidirectional, and exponential anisotropic theoretical semivariogram models, respectively) considered in the two times 10-fold cross-validation study in the derivation of M^{C}_{64} are plotted in gray and black, respectively.

on the forecasting and resubstitution accuracy of the respective correction models. Figs. 6–9 also reveal that the choice of optimized hyperparameters is not universal. In particular, the optimized LASSO parameters for the derivation of M^{P}_{64} and M^{P}_{161} are 0.9 and 0.4, respectively, and the optimal theoretical semivariogram models for the derivation of M^{C}_{64} and M^{C}_{161} are the exponential anisotropic and linear omnidirectional models, respectively. Subsequently, the results of the cross validation study in the derivations of M are presented in Figs. 10 and 11, based on which the optimized value of w^{P}, denoted by $\hat{w}^{P}$, is estimated. $\hat{w}^{P} = 0.65$ indicates that the decision to incorporate information about the spatial correlation in OTWTs among neighboring reforming tubes into M improves its forecasting accuracy and, therefore, justifies the design of the statistical-based model identification. These findings suggest that two times 10-fold cross validation is a reliable accuracy estimation technique to obtain the optimized hyperparameters from the reformer database in a sense that it assesses and compares the forecasting performance of CV data-driven models derived from all given choices of hyper-

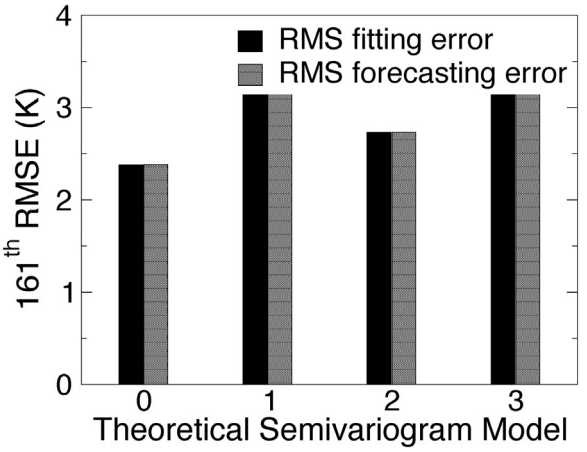

Fig. 9 – RMS fitting and forecasting errors associated with each of the four theoretical semivariogram models (given on the horizontal axis as 0, 1, 2, and 3, which correspond to linear omnidirectional, linear anisotropic, exponential omnidirectional, and exponential anisotropic theoretical semivariogram models, respectively) considered in the two times 10-fold cross-validation study in the derivation of M^{C}_{161} are plotted in gray and black, respectively.

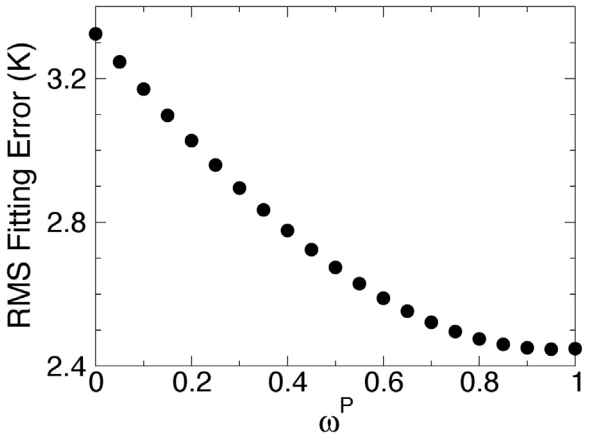

Fig. 10 – RMS fitting errors associated with the proposed values of w^{P} generated from the two times 10-fold cross-validation study in the derivation of M are plotted in black circles.

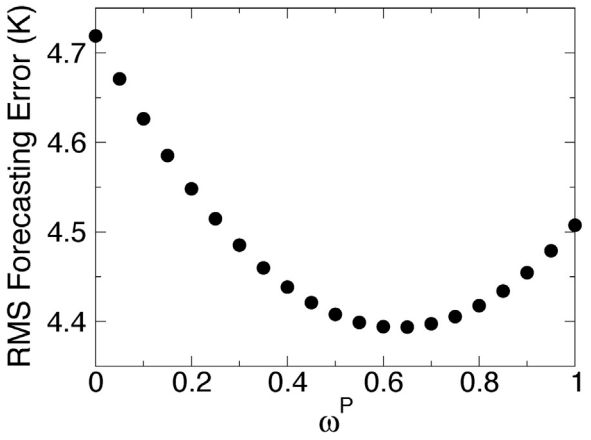

Fig. 11 – RMS fitting errors associated with the proposed values of w^{P} generated from the two times 10-fold cross-validation study in the derivation of M are plotted in black circles.

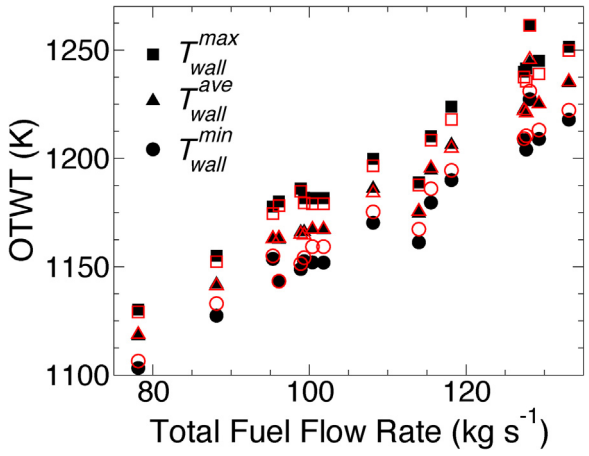

Fig. 12 – Comparison of the maximum, average and minimum values in the OTWT distribution between the plant data (represented by filled black symbols) and the corresponding estimate computed by *M* (represented by the empty red symbols) at varying total fuel flow rates. In Fig. 12, we use jitter to add a small uniform random number on the range from −2% to 2% of the original total flow rate to itself for visual clarity.

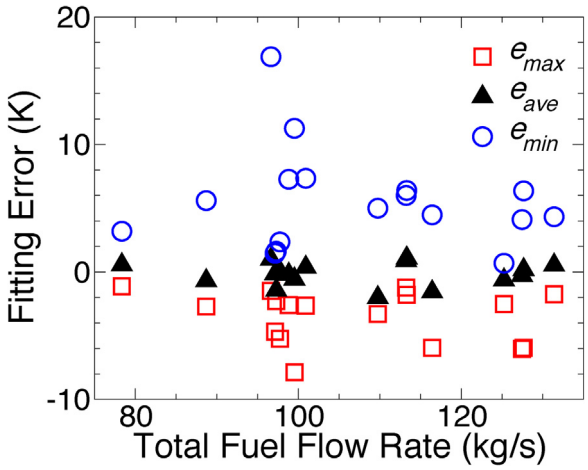

Fig. 13 – Fitting errors of the maximum, average and minimum OTWTs between the estimated OTWT distribution, which is computed using the plant inputs and *M*, and the corresponding plant data. In Fig. 13, we use jitter to add a small uniform random number on the range from −2% to 2% of the original total flow rate to itself for visual clarity.

parameters on the basis of root mean square (RMS) errors with low bias. In addition, this evidence suggests that all hyperparameters used in the derivation of *M* must be independently and optimally selected.

In the remainder of this subsection, we demonstrate that *M*, which is derived with the optimized hyperparameters estimated from the presented cross-validation studies and the reformer database, has an excellent resubstitution accuracy using the fitting errors as a metric. Fig. 12 shows that the descriptive statistics, i.e., the maximum, average and minimum OTWTs, of the estimated OTWT distribution, which is calculated by using the documented reformer fuel inputs and *M*, are consistent with those of the respective plant data in the reformer database. Specifically, the maximum deviations of the maximum, average and minimum OTWTs between the estimated OTWT distribution and the corresponding plant data are 7.9 K, 2.0 K and 16.9 K, respectively, and are considered to be negligible with respect to the magnitude of the OTWTs. Fig. 12 also reveals that *M* exhibits a common characteristic of interpolation methods, i.e., ordinary Kriging, in which the maximum OTWTs are underestimated, while the minimum OTWTs are overestimated. In addition, due to the use of a sufficiently large training set, i.e., more than 25 data sets, in the derivation of *M*, the central limit theorem (CLT) can be used to get a quantitative assessment of the fitting errors of the maximum, average and minimum OTWTs between the estimated OTWT distribution and the corresponding plant data. In particular, the mean residual ($\bar{e}_j$) and residual standard error (s_j) of the descriptive statistics estimated by *M* can be computed as follows,

$$\bar{e}_j = \frac{1}{N}\sum_{i=1}^{N} e_j^i \tag{20a}$$

$$s_j^2 = \frac{1}{N-1}\sum_{i=1}^{N}\left(e_j^i - \bar{e}_j\right)^2 \tag{20b}$$

where *j* represents different types of the descriptive statistics, e.g., *j* is *max*, *min* and *ave*, and *N* is the number of data sets in the reformer database. It is found that the estimated maximum OTWT from *M* has the mean residual of −3.2 K and the residual standard error of 3.8 K, the estimated minimum OTWT from *M* has the mean residual of 5.2 K and the residual standard error of 17.6 K, and the estimated average OTWT from *M* has the mean residual of −0.03 K and the residual standard error of 0.72 K as shown in Fig. 13. This finding and the feature of *M* must be accounted for in the formulation of the model-based balancing procedure that aims to maximize the conversion of methane via SMR within the physical limitation of the reforming tube wall material. Next, we wish to demonstrate that *M* can also generate adequately accurate estimates for all reforming tubes inside the reformer in addition to the maximum, average and minimum values of the OTWT distribution. In this effort, we create two heat maps of the OTWT distribution from the estimates generated by using *M* and the optimized reformer fuel input at the nominal total fuel flow rate (as shown in Fig. 14(a)) and from the corresponding plant data (as shown in Fig. 14(b)) to visually assess the resubstitution accuracy of *M*. Fig. 14 shows that the hot and cold regions in the estimated OTWT distribution are consistent with those in the corresponding plant data. This evidence indicates that *M* derived by the statistical-based model identification with the optimized hyperparameters estimated from the two times 10-fold cross-validation studies is the reliable model for the OTWT distribution. Therefore, *M* can be used to create the furnace-balancing optimizer to determine the optimized flow control valve distribution that aims to minimize the degree of nonuniformity in the OTWT distribution at any given total fuel flow rate.

8.2. *Dynamic response of the reformer*

In this subsection, the transient response of the reformer, and particularly, the OTWT distribution, is investigated when the total fuel flow rate is increased to increase the plant throughput, and based on which we design the appropriate strategy to implement to the maximized total fuel flow rate estimated

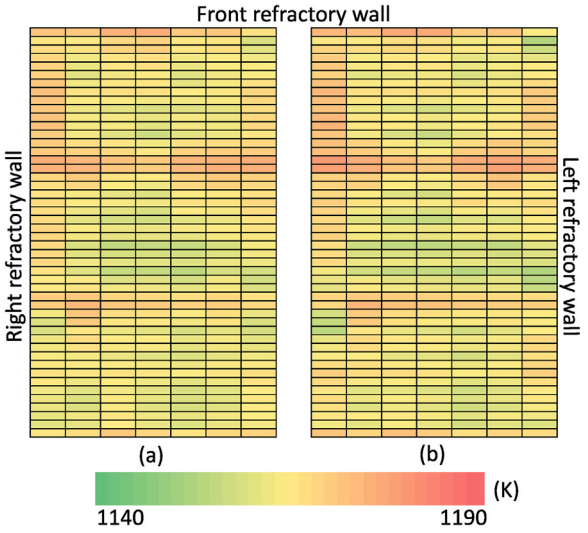

Fig. 14 – Comparison of the estimated OTWT distribution (a), which is generated by using *M* and the optimized reformer fuel input at the nominal total fuel flow rate, to the respective plant data (b). In Fig. 14, each cell represents a unique reforming tube, the location of each cell in the table corresponds to that of the respective reforming tube in the combustion chamber, of which orientation can be visualized by the keywords along the edges and Fig. 2, and the color of each cell represents the value of the respective OTWT, which is specified by the colorbar. (For interpretation of the references to color in this figure legend, the reader is referred to the web version of the article.)

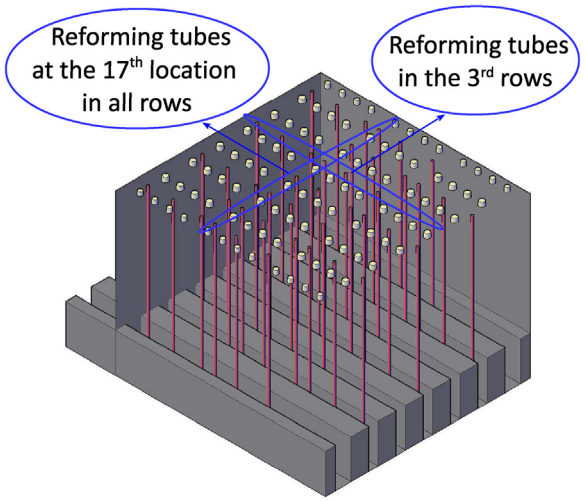

Fig. 15 – Isometric view of the reformer in which the right and back refractory walls are made transparent to display the reforming tubes of which OTWTs at a fixed distance of 6.5 m away from the reformer ceiling are monitored to track the convergence progress of the transient simulations of the reformer CFD model.

Table 1 – Comparison of representatives of the monitored transport variables documented at the last sampling time in the transient simulation of the reformer that is subjected to the positive step change of 21.6 kg s^{-1} in the total fuel flow rate from the nominal value to those extracted from the converged solutions of the corresponding steady-state simulation.

	Steady-state solution	Transient solution	Percent deviation (%)
T^{96}_{wall} (K)	1213.8	1214.7	0.1
T^{103}_{wall} (K)	1205.6	1205.0	0.0
T^{111}_{wall} (K)	1219.5	1219.7	0.0
T^{112}_{wall} (K)	1217.6	1217.9	0.0
T^{119}_{wall} (K)	1203.9	1203.7	0.0
T^{127}_{wall} (K)	1215.4	1214.4	0.1
T^{16}_{wall} (K)	1212.7	1213.0	0.0
T^{64}_{wall} (K)	1217.9	1218.0	0.0
T^{160}_{wall} (K)	1215.0	1213.7	0.1
T^{208}_{wall} (K)	1219.0	1217.7	0.1
T^{256}_{wall} (K)	1221.0	1222.3	0.1
$\|T^{1}_{wall}\|_{\infty}$ (K)	1245.9	1246.1	0.0
$\|T^{63}_{wall}\|_{\infty}$ (K)	1254.0	1254.6	0.0
$\|T^{127}_{wall}\|_{\infty}$ (K)	1248.7	1247.1	0.1
$\|T^{191}_{wall}\|_{\infty}$ (K)	1265.8	1265.3	0.0
$\|T^{223}_{wall}\|_{\infty}$ (K)	1245.2	1246.3	0.1
$\|T^{251}_{wall}\|_{\infty}$ (K)	1233.2	1233.8	0.0
$\|T^{288}_{wall}\|_{\infty}$ (K)	1253.6	1249.0	0.4
$\bar{x}_{H_2}$	0.320	0.320	0.0
$\bar{x}_{H_2O}$	0.500	0.500	0.0

by the furnace-balancing scheme. To this end, we propose two case studies in which the total fuel flow rate is increased by ~2% (1.8 kg s^{-1}) and ~22% (21.6 kg s^{-1}), respectively, from the nominal flow rate of 98.133 kg s^{-1}. In both cases, the optimized valve distribution identified in Tran et al. (2017a) is used to distribute the total flow rate in the reformer operated at higher capacities, and the steady-state solution generated by the reformer CFD model at the nominal total fuel flow rate and the corresponding optimized valve distribution is used as the initial condition. Subsequently, ANSYS Fluent parallel solver with the explicit step size of 0.5 s and the max iterations per time step of 100 (determined by trial and error) is used to obtain the transient response of the reformer CFD model to step inputs. It is important to note that the predefined max iteration per time step must be sufficiently large so that the ANSYS Fluent parallel solver can iterate to convergence, which is defined by the global normalized residuals of conserved variables of which values are strictly smaller than 10^{-5}, within each time step for a given predefined step size. In an effort to track the convergence progress of the transient simulations of the reformer CFD model, we monitor the mole fractions of hydrogen and unreacted steam in the synthesis gas of the reformer, the OTWTs at a fixed distance of 6.5 m away from the reformer ceiling of 42 representative reforming tubes and the maximum OTWTs across the reforming tube length of a few selected reforming tubes as shown in Fig. 15. A transient simulation of the reformer CFD model subjected to a step increase in the total fuel flow rate is said to reach convergence when the monitored transport variables fully relax to the steady-state values. In addition, to validate the transient solutions acquired by solving the reformer CFD model with ANSYS Fluent transient solver, we will compare the monitored transport variables recorded at the last sampling time in the transient simulations to those extracted from the converged solutions of the corresponding steady-state simulations.

In the remainder of this subsection, the transient response of the monitored transport variables to the deterministic step changes in which the total fuel mass flow rate is increased by 1.8 and 21.6 kg s^{-1}, respectively, is presented as shown in Table 1 and Figs. 16–20. Table 1 shows that the steady-state values of the monitored transport variables generated by the transient simulations are consistent with those generated by the steady-state simulations, which confirms that the physical time of 400 s is sufficient for the transient simulations of the reformer CFD model subjected to a step increase in the

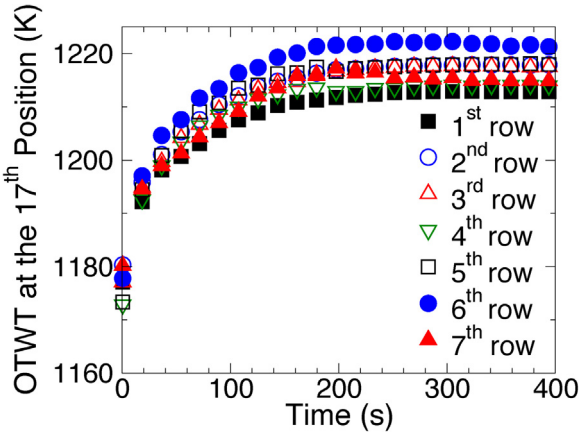

Fig. 16 – The transient response of the OTWTs at a fixed distance of 6.5 m away from the reformer ceiling of the reforming tubes at the 17th position across all rows inside the combustion chamber as shown in Fig. 15 to a positive step change of 21.6 kg s^{-1} in the total fuel flow rate from the nominal value.

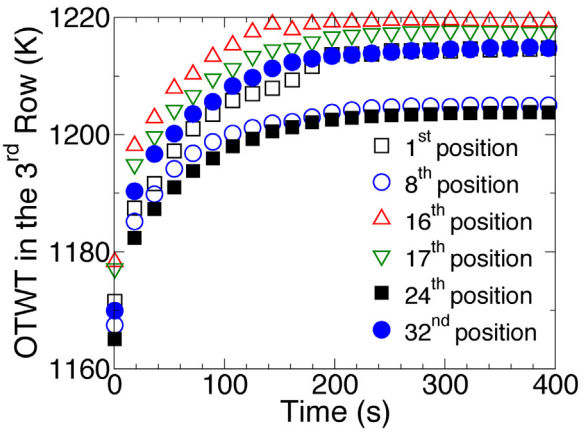

Fig. 17 – The transient response of the OTWTs at a fixed distance of 6.5 m away from the reformer ceiling of six representative reforming tubes along the 3rd row inside the combustion chamber as shown in Fig. 15 to a positive step change of 21.6 kg s^{-1} in the total fuel flow rate from the nominal value.

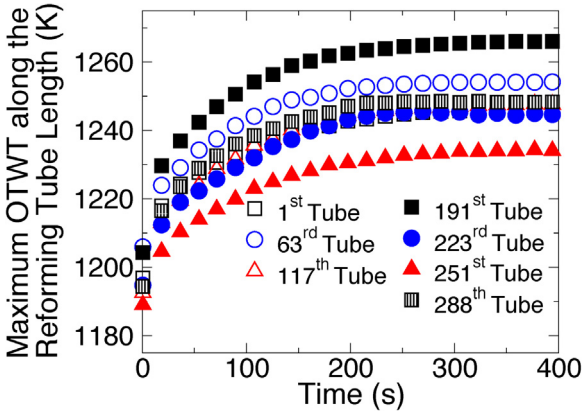

Fig. 18 – Transient response of the maximum OTWTs across the reforming tube length of seven representative reforming tubes at different regions inside the combustion chamber to a positive step change of 21.6 kg s^{-1} in the total fuel flow rate from the nominal value.

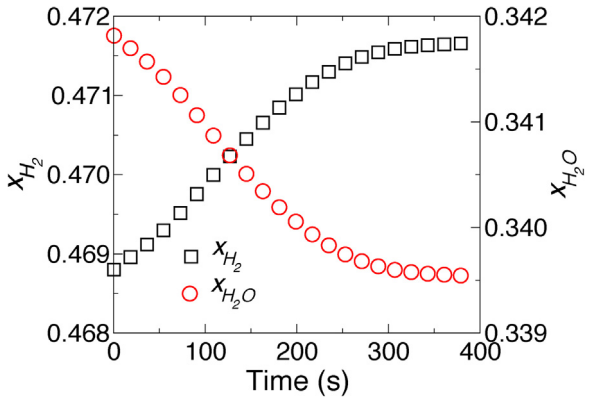

Fig. 19 – Transient response of the hydrogen and unreacted steam mole fractions in the synthesis gas to a positive step change of 1.8 kg s^{-1} in the total fuel flow rate from the nominal value.

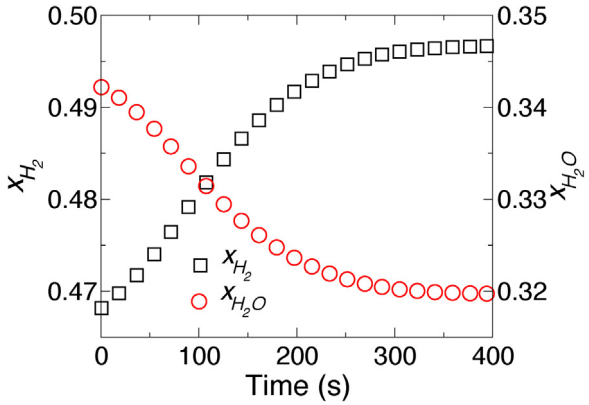

Fig. 20 – Transient response of the hydrogen and unreacted steam mole fractions in the synthesis gas to a positive step change of 21.6 kg s^{-1} in the total fuel flow rate from the nominal value.

total fuel flow rate at $t = 0$ s to reach steady-state. Specifically, the transient response (shown in Figs. 16–20) and steady-state values (shown in Table 1) of the monitored transport variables indicate that the reformer reaches steady-state within ~350 s, and the reformer time constant is independent of the magnitude of the step increase in the total fuel flow rate. It is also interesting to note that the reformer time constant is expected to be insensitive to operational disturbances associated with flow control valves because the disturbances considered in this study can only affect the reformer fuel input, e.g., stuck valves may cause the spatial distribution of the optimized reformer fuel input inside the reformer to become nonoptimal. In addition, the transient response of the OTWTs at a fixed distance of 6.5 m away from the reformer ceiling shown in Figs. 16 and 17 and the transient response of the maximum OTWTs across the reforming tube length shown in Fig. 18 exhibit characteristics of first-order systems in which the initial rates of change are the largest, and the monitored OTWTs monotonically reach the new steady-state values. The prior can be explained by the rapid combustion of the furnace-side fuel coupled with fast thermal radiative heat transfer in the high temperature combustion chamber, which allows the reforming tubes to instantaneously experience the step increase in the total fuel flow rate. While the latter is believed to be the result of rapid energy consumption due to the endothermic SMR in the tube side, which prevents the accumulation of thermal energy in the reforming tube wall and,

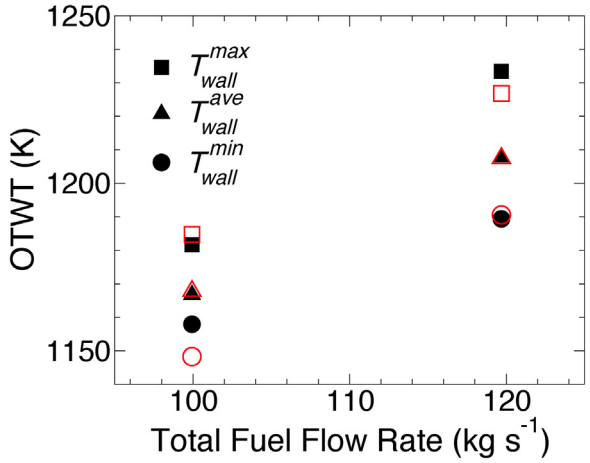

Fig. 21 – Comparison of the maximum, average and minimum values in the OTWT distribution between the plant data (represented by filled black symbols) and the corresponding forecasting estimate (represented by the empty red symbols) computed by M, the two proposed total fuel flow rates and the optimized valve distribution identified in Tran et al. (2017a). (For interpretation of the references to color in this figure legend, the reader is referred to the web version of the article.)

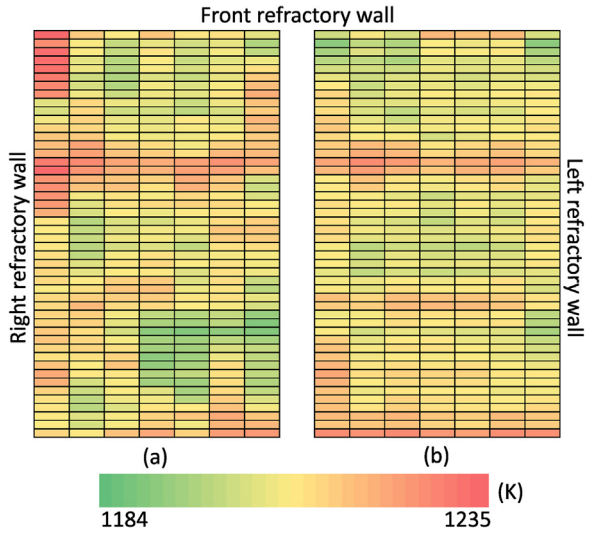

Fig. 22 – Comparison of the estimated OTWT distribution (a), which is generated by using M, the proposed total fuel flow rate for the second case study and the optimized valve distribution identified in Tran et al. (2017a), to the respective plant data (b). In Fig. 22, each cell represents a unique reforming tube, the location of each cell in the table corresponds to that of the respective reforming tube in the combustion chamber, of which orientation can be visualized by the keywords along the edges and Fig. 2, and the color of each cell represents the value of the respective OTWT, which is specified by the colorbar. (For interpretation of the references to color in this figure legend, the reader is referred to the web version of the article.)

therefore, dismisses all possibility to observe the overshoot response of OTWTs. To the contrary, the transient response of the hydrogen and unreacted steam mole fractions in the synthesis gas as shown in Figs. 19 and 20 exhibits characteristics of overdamped second order systems, in which the monitored mole fractions reach the new steady-state values without oscillatory; however, the largest rates of change occur well after $t = 0$ s, e.g., $t = 50$ s. This observation can be justified by the thermal resistance of the reforming tube walls and of the catalyst network. The analysis of the transient response of the monitored transport variables in the proposed case studies supports the assumption that upon a step increase in the total fuel flow rate, the maximum OTWT across the reforming tube length of each reforming tube is expected to monotonically approach its steady-state value without overshoot. The assumption implies that the optimized reformer fuel input predicted by the furnace-balancing scheme in a sense that the steady-state values of the maximum OTWTs across the reforming tube length of all reforming tubes are approaching the design temperature of the reforming tube wall can be implemented in a step change fashion without burning out the reforming tubes. In addition, the transient solutions are valuable resources, which allows us to quantitatively assess the forecasting accuracy of M (derived with the optimized hyperparameters estimated from the cross-validation studies and the reformer database) using the forecasting errors as a metric. Fig. 21 shows that the forecasting errors of the descriptive statistics between the estimated OTWT distribution, which is calculated by using M and the reformer fuel inputs proposed for the investigation of the reformer dynamic behavior, and the corresponding OTWT distribution, which is documented at the last sampling time in the transient simulations, are within two residual standard error from the mean residual of the respective quantities. Specifically, the maximum residuals of the maximum, average and minimum OTWTs between the estimated OTWT distribution and the corresponding plant data are 6.6 K, 1.1 K and 9.6 K, respectively. Fig. 22 shows that the contour heat map of the estimated OTWT distribution generated by using M and the reformer fuel input designed for the second transient case study (as shown in Fig. 22(a)) has similar features (e.g., locations of the hot and cold regions) to that of the corresponding OTWT distribution documented at the last sampling time in the transient simulation (as shown in Fig. 22(b)). This analysis justifies the assumption that M is the accurate model for the OTWT distribution in Section 8.1. Therefore, it can be stated with high certainty that in the reformer operated under the optimized total fuel flow rate and the corresponding optimized valve distribution predicted by the furnace-balancing scheme, the steady-state values of the maximum OTWTs across the reforming tube length of all reforming tubes are expected to be strictly less than the design temperature of the reforming tube wall.

8.3. *Validation of the furnace-balancing scheme*

In this subsection, we evaluate the performance of the balancing procedure under the following assumptions: all flow control valves in the reformer are operational, the initial total fuel flow rate of 98.133 kg s^{-1} is optimally distributed with the optimized valve distribution reported in Tran et al. (2017a,b), and the design OTWT of the reforming tube wall (denoted by T_{wall}^{design}) taken from typical plant data has a value of 1300 K. To this end, we propose a systematic approach to estimate the maximum allowable OTWT, which is a critical parameter of the furnace-balancing scheme because $T_{wall}^{max,*}$ directly controls the maximum total fuel flow rate and, therefore, the respective optimized valve distribution estimated by the proposed approach. Initially, a deliberate review of the results documented in Tran et al. (2017a,b) reveals that the maximum OTWT along the reforming tube length among all reform-

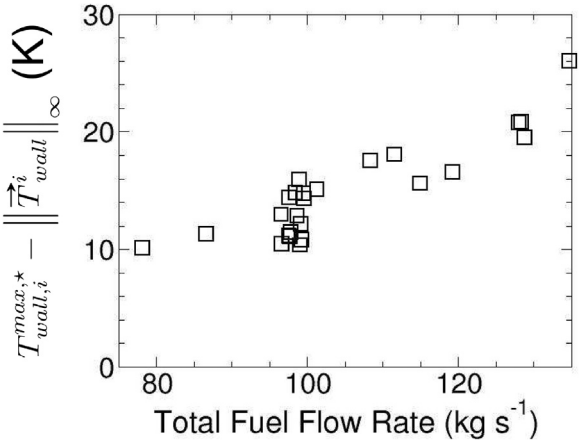

Fig. 23 – Temperature difference between the maximum OTWT along the reforming tube length among all reforming tube ($T_{wall}^{max,\star}$) and the maximum value of the OTWT distribution ($T_{wall}^{max,*}$) when the reformer is operated under varying total fuel flow rates and varying valve distributions.

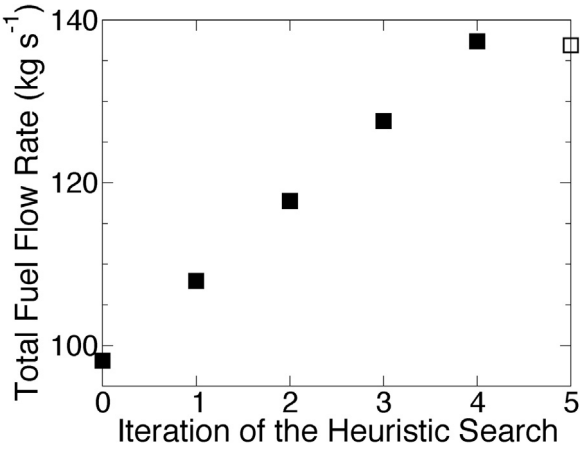

Fig. 24 – Total fuel flow rate generated by the aggressive flow rate generator (represented by the filled symbols) and by the conservative flow rate generator (represented by the empty symbols) in an effort to determine the maximized total fuel flow rate to achieve the desired reformer firing rate without causing premature failure of the reforming tubes.

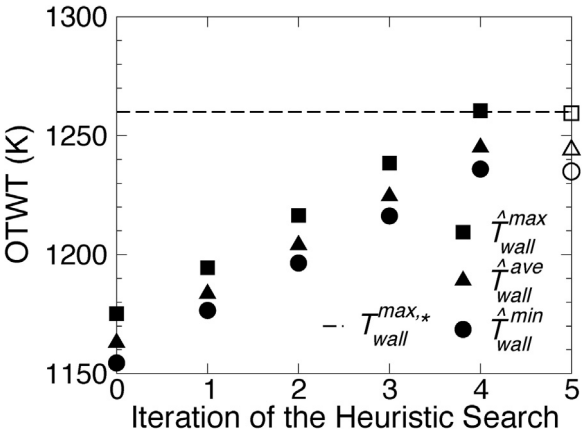

Fig. 25 – Maximum, average and minimum values of the estimated OTWT distribution, which is computed using *M* with the total fuel flow rate and the respective optimized valve distribution proposed by the aggressive search (represented by the filled symbols) and by the conservative search (represented by the empty symbols) in the process of estimating the maximized total fuel flow rate to achieve the desired reformer firing rate without causing premature failure of the reforming tubes.

ing tubes (denoted by $T_{wall}^{max,\star}$) does not necessarily occur in the OTWT distribution at a location 6.5 m from the reformer ceiling. In fact, the reformer database indicates that $T_{wall}^{max,\star}$ is always larger than the maximum value in the OTWT distribution as shown in Fig. 23. This finding suggests that if the reformer were to be operated under the total fuel flow rate that permitted the maximum value in the OTWT distribution to be near T_{wall}^{design}, $T_{wall}^{max,\star}$ would undoubtedly exceed T_{wall}^{design}, which would accelerate the degradation of the microstructure inside the reforming tube wall and cause the reforming tubes to rupture prematurely. Furthermore, as the maximum total fuel flow rate and the respective optimized valve distribution calculated with the furnace-balancing scheme is implemented in an open-loop control fashion in this work, it is necessary to also account for plant-model mismatch in the estimation of $T_{wall}^{max,*}$. Specifically, the residual analysis of the fitting errors of the data-driven model for the OTWT as presented in Section 8.1 provides an efficient means to estimate plant-model mismatch; as a result, $T_{wall}^{max,*}$ can be determined as follows,

$$T_{wall}^{max,*} = T_{wall}^{design} - \max_{1\le i\le 26}\left\{T_{wall,i}^{max,\star} - \|\vec{T}_{wall}^{i}\|_{\infty}\right\} - (\bar{e}_{max} + 2.5 s_{max}), \quad (21)$$

and $T_{wall}^{max,*}$ is found to be ~1260 K. Then, we execute the balancing procedure on our shared computational resources on the Hoffman2 computing cluster. The CPU clock time of a high performance computing core on the Hoffman2 computing cluster devoted for the balancing procedure to optimize the total fuel flow rate and its spatial distribution inside the reformer to maximize the methane conversion via SMR without violating the physical limitation of the reforming tube wall material is only on the order of a few minutes. This evidence highlights the potential of the balancing procedure for real-time optimization of the reformer to improve the plant-wise energy efficiency and to perform load alterations as well as to reject operational disturbances associated with flow control valves.

In the remainder of this subsection, the results generated from the balancing procedure under the predefined assumptions and $T_{wall}^{max,*}$ of 1260 K are presented as shown in Figs. 24 and 25. Specifically, Figs. 24 and 25 indicate that under the initial total fuel flow rate of 98.133 kg s^{-1} optimally distributed with the respective valve distribution, $\hat{T}_{wall,0}^{max}$ is equal to 1175.25 K, which is smaller than $T_{wall}^{max,*}$; therefore, $\hat{T}_{wall,0}^{max}$ allows the aggressive search recursively to apply large increments to the total fuel flow rate to determine the smallest upper-bound value. In addition, Figs. 24 and 25 show that in the 4th iteration of the aggressive search, $F_{tot}^{4,1}$ of 137.4 kg s^{-1} is identified as the smallest upper-bound value because $\hat{T}_{wall,4}^{max,1}$ is equal to 1260.5 K and is greater than $T_{wall}^{max,*}$. Furthermore, Figs. 24 and 25 show that the conservative search gradually applies small decrements to the upper-bound value, and in the 1st iteration of the conservative search, $F_{tot}^{1,2}$ of 136.896 kg s^{-1} is identified as the optimized total fuel flow rate because $\hat{T}_{wall,1}^{max,2}$ begins to fall below $T_{wall}^{max,*}$ indicating that the reformer has returned into the safe operating regime. Finally, in the main layer of the furnace-balancing scheme, F_{tot}^{op} and the $\vec{V}^{op}$ are translated into $\vec{F}^{op}$, which is applied as the reoptimized burner boundary conditions for the reformer CFD model in a step

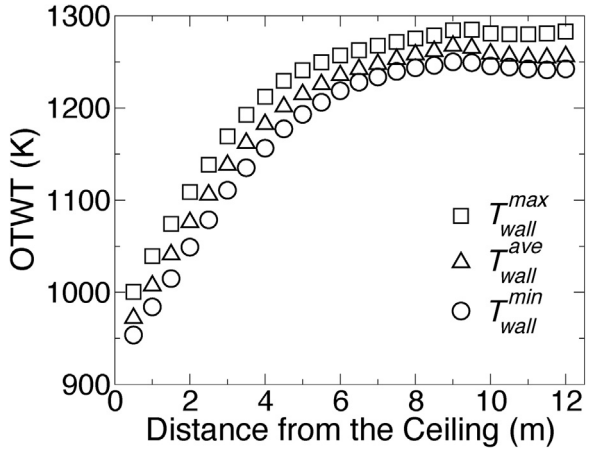

Fig. 26 – Maximum, average and minimum OTWT profile along the reforming tube length among all reforming tubes generated by the reformer CFD model in which the boundary conditions are adjusted based on the maximized total fuel flow rate and the corresponding optimized valve distribution that are identified by the balancing procedure.

increase fashion, and the results are presented as shown in Fig. 26. Specifically, Fig. 26 indicates that $T_{wall}^{max,\star}$ is 1288.35 K, which is less than T_{wall}^{design}, and, therefore, justifies that a positive step change of 38.763 kg s^{-1}, which is equivalent to ~39.5% increase from the nominal value, in the total fuel flow rate can be applied to achieve the optimized firing rate without accelerating the degradation of the microstructure of the reforming tube wall.

9. Conclusion

In this work, a furnace-balancing scheme that simultaneously searches for the optimized total fuel flow rate and the respective optimized valve distribution to increase the methane conversion via SMR without accelerating the degradation of the microstructure of the reforming tube wall material was proposed. To this end, a high fidelity CFD model for the reformer, assumed to represent the on-line unit at an SMR-based hydrogen facility, was used to characterize the previously unstudied dynamic behavior of the reformer. Specifically, the reformer that was initially operated under the nominal total fuel flow rate and the respective optimized valve distribution was subjected to two deterministic step changes in the total fuel flow rate. The corresponding evolution of the mole fractions of hydrogen and unreacted steam in the synthesis gas, the OTWTs at a fixed distance of 6.5 m away from the reformer ceiling and the maximum OTWTs across the reforming tube length of a few selected reforming tubes was analyzed, based on which positive step changes in the total fuel flow rate to achieve the optimized firing rate in the reformer were deemed appropriate. It is important to note that the transient simulations of the reformer CFD model were only computationally feasible with the use of 7 private-access high performance compute nodes with the total processing power of 128 cores and system memory of 1640 GB on the Hoffman2 computing cluster.

Then, the furnace-balancing framework, the statistical-based model for the OTWT distribution and the valve-to-flow rate converter developed in our previous work were integrated with the heuristic search algorithm to design the robust balancing procedure. In the balancing procedure, a series of computing tasks is executed to estimate the maximum value of the initial OTWT distribution based on information from the initial reformer input. This information and the user-defined maximum allowable OTWT are used to guide the aggressive search to identify the neighborhood of the optimal total fuel flow rate and, subsequently, the conservative search to identify the optimized value of the optimal total fuel flow rate such that the operational specifications are satisfied. The optimized total fuel flow rate and the corresponding optimized valve distribution were used to adjust the boundary conditions of the reformer CFD model, and the results demonstrated that the optimized total fuel flow rate could be increased from 98.133 to 136.896 kg s^{-1} in a step change fashion without accelerating the degradation of the microstructure of the reforming tube wall.

References

Alvino, A., Lega, D., Giacobbe, F., Mazzocchi, V., Rinaldi, A., 2010. Damage characterization in two reformer heater tubes after nearly 10 years of service at different operative and maintenance conditions. Eng. Fail. Anal. 17, 1526–1541.

Balat, M., 2008. Potential importance of hydrogen as a future solution to environmental and transportation problems. Int. J. Hydrogen Energy 33, 4013–4029.

Bane, S.P.M., Ziegler, J.L., Shepherd, J.E., 2010. Development of One-Step Chemistry Models for Flame and Ignition Simulations, Technical Report. GALCIT Report GALCITFM:2010.002.

Barreto, L., Makihira, A., Riahi, K., 2003. The hydrogen economy in the 21st century: a sustainable development scenario. Int. J. Hydrogen Energy 28, 267–284.

Cressie, N., 1985. Fitting variogram models by weighted least squares. J. Int. Assoc. Math. Geol. 17, 563–586.

Ding, Y., Alpay, E., 2000. Adsorption-enhanced steam-methane reforming. Chem. Eng. Sci. 55, 3929–3940.

Gong, J.M., Tu, S.T., Yoon, K.B., 1999. Damage assessment and maintenance strategy of hydrogen reformer furnace tubes. Eng. Fail. Anal. 6, 143–153.

Guan, K., Xu, H., Wang, Z., 2005. Analysis of failed ethylene cracking tubes. Eng. Fail. Anal. 12, 420–431.

Hoeting, J.A., Madigan, D., Raftery, A.E., Volinsky, C.T., 1999. Bayesian model averaging: a tutorial. Stat. Sci. 14, 382–401.

Kumar, A., Baldea, M., Edgar, T.F., Ezekoye, O.A., 2015. Smart manufacturing approach for efficient operation of industrial steam-methane reformers. Ind. Eng. Chem. Res. 54, 4360–4370.

Lao, L., Aguirre, A., Tran, A., Wu, Z., Durand, H., Christofides, P.D., 2016. CFD modeling and control of a steam methane reforming reactor. Chem. Eng. Sci. 148, 78–92.

Latham, D.A., McAuley, K.B., Peppley, B.A., Raybold, T.M., 2011. Mathematical modeling of an industrial steam-methane reformer for on-line deployment. Fuel Process. Technol. 92, 1574–1586.

Lemus, R.G., Duart, J.M.M., 2010. Updated hydrogen production costs and parities for conventional and renewable technologies. Int. J. Hydrogen Energy 35, 3929–3936.

Maximov, A., 2012. Thesis for the Degree of Doctor of Science: Theoretical Analysis and Numerical Simulation of Spectral Radiative Properties of Combustion Gases in Oxy/air-fired Combustion Systems. Lappeenranta University of Technology.

Mishra, S.C., Prasad, M., 1998. Radiative heat transfer in participating media – a review. Sadhana 23, 213–232.

Nicol, D.G., 1995. A Chemical Kinetic and Numerical Study of NOx and Pollutant Formation in Low-emission Combustion (PhD Thesis). University of Washington.

Olivieri, A., Vegliò, F., 2008. Process simulation of natural gas steam reforming: fuel distribution optimisation in the furnace. Fuel Process. Technol. 89, 622–632.

Pantoleontos, G., Kikkinides, E.S., Georgiadis, M.C., 2012. A heterogeneous dynamic model for the simulation and

optimisation of the steam methane reforming reactor. Int. J. Hydrogen Energy 37, 16346–16358.
Peng, X., 2012. Analysis of the thermal efficiency limit of the steam methane reforming process. Ind. Eng. Chem. Res. 51, 16385–16392.
Simpson, A.P., Lutz, A.E., 2007. Exergy analysis of hydrogen production via steam methane reforming. Int. J. Hydrogen Energy 32, 4811–4820.
Tran, A., Aguirre, A., Crose, M., Durand, H., Christofides, P.D., 2017a. Temperature balancing in steam methane reforming furnace via an integrated CFD/data-based optimization approach. Comput. Chem. Eng. 104, 185–200.
Tran, A., Aguirre, A., Durand, H., Crose, M., Christofides, P.D., 2017b. CFD modeling of a industrial-scale steam methane reforming furnace. Chem. Eng. Sci. 171, 576–598.
Tran, A., Pont, M., Aguirre, A., Durand, H., Crose, M., Christofides, P.D., 2018. Bayesian model averaging for estimating the spatial temperature distribution in a steam methane reforming furnace. Chem. Eng. Res. Des. 131, 465–487.
Xu, J., Froment, G.F., 1989. Methane steam reforming, methanation and water-gas shift: I. Intrinsic kinetics. AIChE J. 35, 88–96.